



# **Can atmospheric chemistry deposition schemes reliably simulate stomatal ozone flux across global land covers and climates?**

Tamara Emmerichs<sup>1</sup>, Abdulla Al Mamun<sup>2</sup>, Lisa Emberson<sup>3</sup>, Huiting Mao<sup>4</sup>, Leiming Zhang<sup>2</sup>, Limei Ran<sup>5</sup>, Clara Betancourt<sup>6</sup>, Anthony Wong<sup>7</sup>, Gerbrand Koren<sup>8</sup>, Giacomo Gerosa<sup>9</sup>, Min Huang<sup>10</sup>, Pierluigi Guaita<sup>9</sup>

<sup>1</sup>Institute of Energy and Climate Systems, Troposphere (ICE-3), Forschungszentrum Jülich, Germany, now at Max-Planck-Institute for Meteorology, Germany

<sup>2</sup>Air Quality Research Division, Science and Technology Branch, Environment and Climate Change Canada, Toronto, Ontario M3H 5T4, Canada

<sup>3</sup>Environment & Geography Department, University of York, York, UK.

<sup>4</sup>Department of Chemistry, State University of New York College of Environmental Science and Forestry, Syracuse, NY, 13210, USA

<sup>5</sup>Resource Assessment Branch, USDA-NRCS-SSRA-RIAD

<sup>6</sup>AXA Konzern AG, Cologne, Germany

<sup>7</sup>Centre for Global Change Science, Massachusetts Institute of Technology, Cambridge, MA, United States of America

<sup>8</sup>Copernicus Institute of Sustainable Development, Utrecht University, Utrecht, the Netherlands

<sup>9</sup>Dep.t of Mathematics and Physics, Catholic University of the Sacred Heart, Brescia, Italy

<sup>10</sup>Earth System Science Interdisciplinary Center, University of Maryland, College Park, MD, USA

*Correspondence to:* Tamara Emmerichs (tamara.emmerichs@gmx.de)



25

## 26 **Abstract**

27 Over the past few decades, ozone risk assessments for vegetation have been developed based on stomatal  $O_3$  flux  
28 since this metric is more biologically meaningful than the traditional concentration-based approaches. However,  
29 uncertainty remains in the ability to simulate stomatal  $O_3$  fluxes accurately. Here, we investigate stomatal  $O_3$   
30 fluxes simulated by six common air pollution deposition models across various land cover types worldwide. The  
31 Tropospheric Ozone Assessment Report (TOAR) database, a large collection of measurements worldwide,  
32 provides hourly  $O_3$  concentration and meteorological data which are used to drive the models at 9 sites. The  
33 models estimated summertime  $O_3$  deposition velocities of between  $0.5 - 0.8 \text{ cm s}^{-1}$ , mostly in agreement with the  
34 literature. Simulations of canopy conductance ( $G_{st}$ ) showed differences between models that varied by land  
35 cover type with correlation coefficients of 0.75, 0.80 and 0.85 for forests, crops and grasslands. The model  
36 differences were determined by especially soil moisture and VPD depending upon the model constructs. Finally,  
37 the range of  $POD_y$  simulations at each site across models was most in agreement for crops ( $3 \text{ to } 11 \text{ mmol } O_3 \text{ m}^{-2}$ )  
38  $<$  forests ( $10 \text{ to } 23 \text{ mmol } O_3 \text{ m}^{-2}$ )  $<$  grasslands ( $24 \text{ to } 26 \text{ mmol } O_3 \text{ m}^{-2}$ ). Nevertheless, ensemble model median  
39 response estimates gave results consistent with the literature in terms of those sites where  $O_3$  damage is most  
40 likely to occur. Overall, this study is an important first step in developing and evaluating tools for broad-scale  
41 assessment of  $O_3$  impact on vegetation within the framework of TOAR phase II.

42

## 43 **1. Introduction**

44 Elevated surface  $O_3$  levels significantly damage vegetation due to the stomatal uptake of  $O_3$  by canopy leaves.  
45 Stomatal uptake of  $O_3$  leads to plant tissue injury which in turn causes changes in metabolic functioning,  
46 reducing photosynthesis and consequently plant growth and productivity (Mills et al., 2011; Emberson, 2020;  
47 Ainsworth et al. 2012; Fuhrer et al., 2016; Grulke and Heath, 2020). Such damage can have significant impacts  
48 on crop yields and quality, leading to economic losses and impacting food security in regions already facing  
49 scarcity (Avnery et al., 2011; Ainsworth et al. 2017; Ramya et al., 2023). There is an ever-growing body of  
50 observational evidence demonstrating a variety of  $O_3$  impacts on different ecosystems (crops, forests, grasslands)  
51 in North America, Europe and more recently, Asia (Emberson 2020). Various indices assessing  $O_3$  exposure to



vegetation have been developed over recent decades with the stomatal  $O_3$  flux ( $POD_y$ ; phytotoxic ozone dose over a threshold  $y$ ) index found to provide better estimates of  $O_3$  risk to vegetation than the more commonly used concentration-based exposure approaches (e.g., Accumulated Ozone over Threshold (AOT); growing season daylight mean  $O_3$  concentration (M7, M12) (Mills et al., 2011; Avnery et al., 2011). A global overview of spatial distribution and trends using concentration-based metrics was provided in the first Tropospheric Ozone Assessment Report (TOAR) by Mills et al. (2018). During TOAR phase II (TOAR-II), here we conduct a flux-based analysis to ensure the most up-to-date vegetation metrics are provided through this community effort.

$O_3$  dry deposition to vegetation is in part determined by canopy-level  $O_3$  concentrations. A significant fraction of  $O_3$  uptake occurs through the plant stomata with the remainder depositing on plant cuticular surfaces and the under-storey vegetation and soil. The stomatal contribution can vary between 50 and 80%, depending on the factors controlling the partitioning of stomatal and non-stomatal uptake (e.g., Huang et al., 2022; Wong et al., 2022; Clifton et al., 2023). As such, quantifying canopy stomatal conductance is important for assessing the mass balance of atmospheric  $O_3$  concentrations and its potential damage to vegetation. Both stomatal and non-stomatal processes can vary with environmental conditions such as humidity, solar radiation, temperature and  $CO_2$  concentration as well as vegetation type and density (Clifton et al., 2020a). The occurrence of soil water deficit can also play a crucial role where soil water stress induces stomatal closure (Lin et al., 2020; Huang et al., 2022). There are two commonly used stomatal conductance ( $g_s$ ) models - the empirical, multiplicative approach first developed by Jarvis (1976) and the semi-mechanistic coupled net photosynthesis-stomatal conductance models ( $A_{net}$ - $g_s$ ). The common Jarvis-type models (e.g. Emberson et al., 2000; Ganzeveld et al., 1995; Zhang et al. 2003), widely applied due to their simplicity and computational efficiency, correct a prescribed maximum stomatal conductance with the multiplication of different environmental factors (e.g., temperature, light, soil water and atmospheric moisture). The  $A_{net}$ - $g_s$  models couple  $g_s$  to plant photosynthesis by calculating the net assimilation of  $CO_2$  and estimating  $g_s$  based on the resulting supply and demand of  $CO_2$  (Farquhar et al., 1980; Goudriaan et al., 1985; Ball et al., 1987).  $A_{net}$ - $g_s$  models involve multiple non-linear dependencies on soil water, humidity and temperature, among other factors defined by measurement constraints (Ball 1987; Leuning et al., 1997). Heterogeneity of stomatal deposition estimates over different land cover types is anticipated, but model uncertainty depends on the representation of the deposition mechanisms, model parameterisation and meteorological inputs (Hardacre et al., 2015; Clifton et al., 2020b; Huang et al., 2022; Khan et al., 2024).

In this study, the stand-alone version of six  $O_3$  deposition schemes, commonly used in climate or air quality models, are assessed with a focus on their stomatal uptake portion and resulting  $POD_y$  calculation. Using



concurrent O<sub>3</sub> concentration and meteorological variable measurement data from the TOAR database enables us to conduct a detailed intercomparison of multiple deposition schemes by avoiding uncertainties arising from using different input data. For this study, various sites have been selected to represent different land cover types and climate regimes around the globe, focusing on sites where observational data are available for O<sub>3</sub> concentration. By assessing the model estimates of stomatal O<sub>3</sub> deposition at these different sites, we aim to identify key differences in model formulation and parameterisation that influence estimates of stomatal O<sub>3</sub> flux and consequent POD<sub>y</sub>. The estimation of the stomatal uptake from water flux measurements taken from the FLUXNET database provides an additional observational constraint as well as an uncertainty estimate at each site.

Furthermore, sensitivity simulations allow us to investigate the variability of stomatal O<sub>3</sub> deposition and plant damage with key input parameters and land cover characteristics. Post hoc, plant damage will be calculated offline based on the POD<sub>y</sub> simulated by different models and flux-response relationships, where appropriate. Ultimately, we aim to understand the key factors driving stomatal O<sub>3</sub> flux and thus POD<sub>y</sub> and assess the O<sub>3</sub>-induced potential for vegetation damage for different land cover types and global regions.

## 2. Methodology

### 2.1 Meteorological and O<sub>3</sub> data from the TOAR-II database

The TOAR-II database (from now on TOAR) contains harmonised measurements of surface O<sub>3</sub> and its important precursors and key meteorological variables that can impact O<sub>3</sub> concentrations and stomatal O<sub>3</sub> uptake. As one of the largest collections of quality-controlled air pollution measurements in the world, it comprises ground-based station measurements of O<sub>3</sub> concentration at more than 22905 sites globally which cover different periods between 1974 and 2023. These have been collected from different O<sub>3</sub> monitoring networks (e.g., Clean Air Status and Trends Network, CASTNET), harmonised and synthesised to enable uniform processing. The data were selected for inclusion in the TOAR database based on an extended quality control; e.g., sites where the measurement technique changed with time have been excluded. Data errors remain but have been shown to have a minor impact (Schultz et al., 2017). The total uncertainty in modern O<sub>3</sub> measurements is estimated to be < 2 nmol/mol (Tarasick et al., 2018). The meteorological data (irradiance, air temperature, relative humidity,



precipitation, air pressure, and wind speed) in the database stems from the fifth generation of ECMWF reanalysis (ERA5) for global climate (Hersbach et al., 2020). Data re-initialisation (of precipitation and radiation, Copernicus Climate Change Service, 2017) is bridged by (linear) interpolation. The Leaf Area Index (LAI) data in the database stems from the MODerate resolution Imaging Spectroradiometer (MODIS). TOAR data is freely, and openly available through a graphical user interface and a representational State Transfer interface (<https://toar-data.fz-juelich.de/api/v2/>, last access: 01.11.2024). The TOAR data centre team is committed to the Findability, Accessibility, Interoperability, and Reusability principles (Wilkinson et al., 2016). The centre aims to achieve the highest standards regarding data curation, archival, and re-use (Schröder et al., 2021). In this study, additional meteorological ERA5 data required by some models were extracted from the MeteoCloud server (<https://datapub.fz-juelich.de/slcs/meteocloud/index.html>) at Forschungszentrum Jülich.

## 2.2 Observation-constrained stomatal conductance

To compare the modelled stomatal conductance with observational information, we prepared model input data at two sites (Hyytiälä, Harvard Forest) from the FLUXNET 2015 dataset (Pastorello et al., 2020), which is openly available under the CC-BY-4.0 data usage licence. Additional vegetation information for the model input (i.e., LAI, canopy height, and crop calendar data) was provided by the site project investigators. Then, we used the canopy-scale stomatal conductance dataset, SynFlux version 2 to estimate  $G_{st}$  for two forest sites, US-Ha1 and FI-Hyy. While in SynFlux version 1, canopy transpiration is assumed to be equal to total latent heat flux SynFlux version 2 improved its previous estimations (Ducker et al., 2018) by using a machine-learning-based method (Nelson et al., 2018) to partition total evapotranspiration into surface evaporation and canopy transpiration. To train quantile random forest models to relate meteorological conditions with water use efficiency (derived from water and carbon fluxes), periods with minimal surface wetness were chosen during the growing season. These models were then used to back-calculate transpiration for the whole growing season. Instead of the total latent heat flux, the resulting transpiration estimate was used as an input to the inverse Penman-Monteith Equation, reducing the potential high bias in the stomatal conductance estimates in SynFlux version 1.



## 2.3 Summary of sites selected for deposition modelling

Nine sites (Table 1) were selected for this modelling work accounting for the following factors: i. geographical spread, including major continents with terrestrial vegetation; ii. land cover/use types, including the plant functional types (PFTs) which are important in terms of economy, food security, or biodiversity and for which we have fairly good knowledge of O<sub>3</sub> impacts; iii. availability of meteorological and O<sub>3</sub> data from the TOAR database; iv. availability of observational data describing stomatal conductance of water vapour ( $g_{wv}$ ) estimated from the FLUXNET measurements (Section 2.2); and v. location proximity to previous experiments that have investigated O<sub>3</sub> impacts on vegetation that can help interpret our model results.

**Table 1. Sites selected for stomatal deposition modelling using data from the TOAR database grouped by continent. Sites that also have FLUXNET data are denoted by ‘FN’ and those with SynFlux data are denoted by ‘SF’.**

Site (TOAR station id, nearest FLUXNET site id)	Location, station altitude from TOAR	Köppen-Geiger climate classification	Vegetation details (LAI, canopy height in m)	Record (measurement heights in m)	References
Europe					
Hyytiälä, Finland (FI00621, FI-Hyy) FN & SF	61.8611 °N, 24.2833 °E, 104 m	Dfc	LAI: 2.9 Height: 23.3	O <sub>3</sub> : 2014 (4) FLUXNET: 1996/04-2013/09 (14)	Chen et al. (2018); Junninen et al. (2009); Visser et al. (2021)
Grignon, France (FR04038, FR-Gri) FN	48.5819 °N, 1.833 °E, 165 m	Cfb	LAI: 4.3 Height: 3.5	O <sub>3</sub> : 2013/2014 (3) FLUXNET: 2004-2014 (2)	Stella et al. (2013)
Castelporzian	41.8894 °N,	Csa	LAI: 6.9	O <sub>3</sub> :	Gerosa et al. (2005,



o, Italy (IT0952A, IT- Cpz)	12.266 °E, 19 m		Height: 14.0	2013/2014 (19.7) FLUXNET: 2013/2014 (10)	2009); Fares et al. (2009, 2012); personal communications with Silvano Fares
Asia					
Amberd, Armenia (AM0001R)	40.3844 °N, 44.2605 °E, 2080 m	BSk (or Dfa)	LAI: 3.9 Height: 1.0	O <sub>3</sub> : 2009/2010 (3)	
Pha Din, Vietnam (VN0001R)	21.5731 °N, 103.5157 °E, 1466.0 m	Cwa	LAI: 6.9 Height: > 10.0	O <sub>3</sub> : 2015- 2017 (12)	Pieber et al. (2023); Bukowiecki et al. (2018); Yen et al. (2013)
North America					
Quabbin Reservoir/Har vard Forest tower, USA (25-015- 4002, US- Ha1) FN & SF	42.2985 °N, - 72.3341 °E, 312 m	Dfb	LAI: 3.0 Height: 24.0	O <sub>3</sub> : 2010- 2012 (2) FLUXNET: 1993-2012 (24)	Clifton et al. (2019, 2020b); Ducker et al. (2018)
Nebraska, USA (31-055- 0032, US- Ne3)	41.3602 °N, - 96.0250 °E, 400 m	Dfa	LAI: 1.7 Height: 2.5	O <sub>3</sub> : 2010 (2) FLUXNET: 2013/04- (0.5)	Amos et al. (2005); Leung et al (2020)
South America					



Huancayo, Peru (PE0001R)	-12.0402 °N, - 75.3209 °E, 3314 m	Cwb	LAI: 3.6 Height: 1.0	O <sub>3</sub> : 2015 (6)	
Africa					
Mt. Kenya, Kenya (KE0001G)	-0.062 °N, 37.297 °E, 3678.0 m	Aw	LAI: 4.2 Height: 1.0	O <sub>3</sub> : 2015 (unknown)	Henne et al. (2008a,b)

147

148 **Table 2. Land cover type, species and growing season (where SGS = start of growing season and EGS =**  
 149 **end of growing season) by site. The equivalent land cover type and soil texture data used by the models**  
 150 **used in this study (Section 2.3) are also shown. MESSy does not consider different land cover types.**  
 151 **Models that do not consider soil type (i.e. do not include an estimate of soil moisture influence on stomatal**  
 152 **deposition) are marked with \*.**

Station site: land cover type (species) and growing season	Web-D O <sub>3</sub> SE	TEMIR*	NOAH- GEM	ZHANG*	CMAQ
<u>Hyytiälä, Finland:</u> evergreen needleleaf forest (Scots pine) SGS=1, EGS=366	evergreen needleleaf forest, loam	evergreen needleleaf boreal forest	evergreen needleleaf forest, organic material	evergreen needleleaf forest	evergreen needleleaf forest, silty loam (peat)
<u>Grignon, France:</u> crops (rapeseed and wheat) SGS=304, EGS=571	winter wheat, loam	C3 crop	crops/grassla nd mosaic, silt loam	crops	crops (wheat), silty loam





<u>Castelporziano, Italy:</u> evergreen broadleaf forest (laurel, abutis, broad-leaved phillyrea, holm oak, pine) SGS=1, EGS=366	evergreen broadleaf forest, loam	Evergreen broadleaf temperate forest	evergreen broadleaf forest, sandy loam	evergreen broadleaf forest	evergreen broadleaf forest, loamy sand
<u>Amberd, Armenia:</u> Grassland, mixed SGS=1, EGS=366	grassland, loam	grassland	grassland, loam	long grassland	grassland, loam
<u>Pha Din, Vietnam:</u> evergreen needleleaf forest SGS=1, EGS=366	evergreen needleleaf forest, loam	evergreen needleleaf temperate forest	evergreen needleleaf forest, clay	evergreen needleleaf forest	evergreen needleleaf forest, clay
<u>Quabbin Reservoir/Harvard Forest tower, USA</u> SGS=93, EGS=312	temperate mixed forest, loam	deciduous broadleaf temperate forest	deciduous broadleaf forest, sandy loam	deciduous broadleaf forest	deciduous broadleaf forest, sandy loam
<u>Nebraska, USA:</u> crops (maize/soybean rotation) SGS=132/148, EGS=278/260	crops (maize, soybean), loam	C3 crop	crops/grassland mosaic, silty clay loam	crops	crops (corn), silty clay loam
<u>Huancayo, Peru:</u> grassland SGS=1, EGS=366	grassland, loam	grassland	grassland, loam	long grassland	grassland, loam
<u>Mt. Kenya, Kenya:</u> grassland, shrublands SGS=1, EGS=366	grassland, loam	grassland	grassland, loam	long grassland	grassland, silty loam

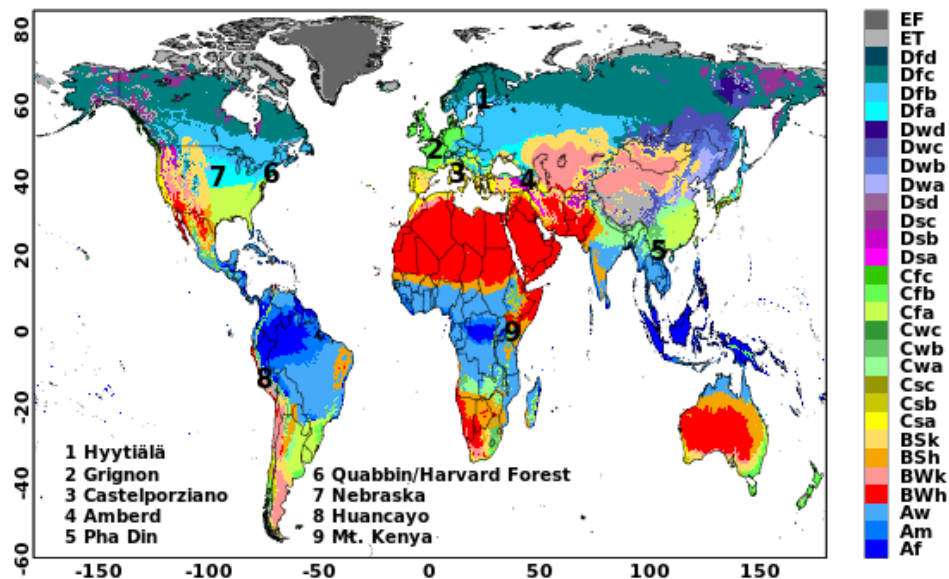


**Fig. 1: Locations of 9 selected sites on Köppen-Geiger climate classification map for 1991-2020 (source: Beck et al., 2023). Table 1 specifies the classifications of these sites.**

### 2.3 Stomatal deposition models and their key inputs

Six widely used empirical/Jarvis and semi-empirical/Ball-Berry types of stomatal deposition models were selected for this study. All of these used models can accommodate a variety of land cover/land use types and provide estimates of stomatal deposition that can be output as both hourly- and season-long cumulative-stomatal deposition metrics. The model details are described below.

- (1) Empirical/Jarvis-type models - The ZHANG model modifying a predefined minimum stomatal resistance for sunny and shaded leaves with environmental stress functions in Jarvis-Style (Zhang et al., 2002; 2003; 2006), the Web-DO<sub>3</sub>SE (i.e., a version of DO<sub>3</sub>SE that is directly coupled to the TOAR database) model modifying a predefined maximum stomatal conductance with phenology and environmental stress functions depending on radiation (PAR), vapour pressure deficit (VPD) and soil water (SM) (Emberson et al. 2000), the CMAQ\_J model modifying a minimum stomatal resistance with stress factors for PAR, air temperature (air T) and relative humidity (RH) at leaf surface, and root zone soil moisture (Pleim and Ran, 2011), the MESSy model instead calculates the initial stomatal



170 conductance based on the PAR (instead of using a stress function) (Ganzeveld et al., 1995; Kerkweg et  
 171 al., 2006)  
 172 (2) Semi-empirical/Ball-Berry - The CMAQ\_P model using linear regression for C3 and C4 plants based  
 173 on CO<sub>2</sub> net assimilation (Ran et al., 2017), the TEMIR model solves the coupled photosynthesis-  
 174 stomatal conductance system (Collatz et al., 1991; Farquhar et al., 1980) separately for sunlit and  
 175 shaded leaves (Tai et al., 2024; Sun et al., 2022) with distinction between C3 and C4 photosynthesis  
 176 (Collatz et al., 1992), the NOAH-GEM model involves additionally RH instead of VPD (Wu et al.,  
 177 2011; Niyogi et al., 2009).

178 All models follow the resistance scheme:

179  $+ \text{---} R_{\text{cut}}$

180 i.e.  $R_a \text{---} R_b \text{---} + \text{---} R_{\text{stom}}$

181  $+ \text{---} R_{\text{inc}} + R_{\text{ground}}$

182 The land cover, growing season, and soil texture specifications used by the models are summarised in Table 2.  
 183 For crops, we used the GGCM Phase 3 crop calendar (Jägermeyr et al., 2021a) which provides the planting date  
 184 and maturity day for 18 different crops at a 0.5° land grid cell resolution (Jägermeyr et al., 2021b). For forest  
 185 trees, we consider four various classes: evergreen-needleleaf (EN), evergreen-broadleaf (EB), deciduous  
 186 needleleaf (DN), and deciduous broadleaf (DB). For evergreen species, we assume a year-round growing season;  
 187 for deciduous species, we used the simple latitude function described in Hayes et al.(2017); and we consider a  
 188 year-round growing season for tropical species. The soil texture categories used by the models were obtained  
 189 from the reference studies in Table 1 and the site principal investigators. Table 3 provides the key formulas,  
 190 input data requirements and references for all models. Key total and stomatal deposition parameters for  
 191 empirical models ( $g_{\text{max}}$ ) and semi-empirical models ( $V_{\text{Cmax}}$ ) are described in Table 4, which gives a good  
 192 indication of the overall difference in the magnitude of stomatal deposition. The models' meteorological and O<sub>3</sub>  
 193 inputs have been introduced in Section. 2.1.

194



195 **Table 3. Stomatal deposition models selected for site-scale modelling (list of symbols: A1 and Section S3 in**  
 196 **the SI, \*uses  $u(h)$ ,  $\alpha_3(h)=1$ , for US-Ne:  $u(h)$ ,  $\alpha_3(h)=0.3$ ).**

Model	Approach	Key Formulas	Key Input data	Reference
ZHANG	Empirical (Jarvis-style)	$R_s = 1 / [G_s(PAR)f(T)f(D)f(\psi) \times D_i/D_v]$ $G_s(PAR) = \frac{L_{sun}}{r_s(PAR_{sun})} + \frac{L_{shade}}{r_s(PAR_{shade})}$ $r_s(PAR) = r_{s,min}(1 + b_{rs}/PAR)$	LAI, LUC, Wspeed, ssrd, T2m, Tskin, RH	Zhang et al., 2002; 2003; 2006
Noah-GEM	Semi-empirical, photosynthesis is-based (Ball-Berry type)	$R_s = 1/[LAI(mA_n h_s P/C_s + b)]$	LAI, LUC, Wspeed, ssrd, strd, T2m, Tskin, RH	Wu et al., 2011; Niyogi et al., 2009
CMAQ-J	Empirical (Jarvis-style)	$R_s = r_{s,min} LAI / (f_{PAR} f_T f_{vpd} f_w)$	LAI, Tair, PAR, ssrd, rn, RH SM	Pleim & Ran 2011
CMAQ-P	Semi-empirical, photosynthesis is-based	$R_s = 1/(m_g A_{net} e_s P_a / C_s e_i + g_0)$	LAI, CO <sub>2</sub> , Pa, u*,	Ran et al., 2017



	(Ball-Berry type)		h_dis, z0,  SM, Tsoil, wspeed , wdir, Soil texture, C3/C4 type, PAR, ssrd, rn, P_rate, sn, sd	
<b>TEMIR</b>	Semi-empirical, photosynthesis-based (Ball-Berry type)	$R_s = 1 / \left[ \left( \frac{L_{sun}}{r_b + r_{sun}} + \frac{L_{shade}}{r_b + r_{shade}} \right) \frac{D_i}{D_v} \right]$ $r_s = 1/g_s = 1 / \left[ \alpha \left( \frac{mA_n \left( \frac{e_s}{e_{sat}} \right)}{\left( \frac{C_s}{P_{atm}} \right)} + b \right) \right]$	LAI, LUC, u*, ssrd, T2m, Tskin, RH, SM	Tai et al., 2024; Sun et al., 2022
<b>MESSy</b>	Empirical (Jarvis-style)	$R_s = [r_s(PAR, LAI) / f_T f_{vpd} f_w] \times D_v / D_i$ $r_s(PAR, LAI) = \frac{kc}{\left[ \frac{b}{d PAR} \ln \left( \frac{d \exp(kLAI) + 1}{d + 1} \right) - \ln \left( \frac{d \exp(-kLAI)}{d + 1} \right) \right]}$	LAI, ssrd, RH, sw, Tir	Emmeric hs et al., 2021; Kerkweg et al., 2006; Ganzevel d et al., 1998



Web-DO <sub>3</sub> SE	Empirical (Jarvis-style)	$r_s = g_{max} \max\{f_{min}, f_{temp}, f_{VPD}, f_{SWC}\} \times f_{phen} \times f_{light}$	Tair, VPD wspeed, P, Pa, O <sub>3</sub> , Gr	Emberso n et al., 2000; Bueker et al., 2012; Simpson et al., 2011; Guaita et al., 2023a
------------------------	--------------------------	--	---	---

197

198

199 **Table 4 Model parameter  $V_{Cmax}$  [in  $\mu\text{mol CO}_2 \text{ m}^{-2} \text{ s}^{-1}$ ] and  $g_{max}$  [O<sub>3</sub> in  $\text{cm s}^{-1}$ ] by land cover/land use type.**  
 200 **Note that the values presented in the table were recalculated from the original respective rsmin values for**  
 201 **H<sub>2</sub>O ( $\text{s m}^{-1}$ ) in ZHANG, MESSy, and CMAQ\_J, and  $V_{Cmax}$  values for O<sub>3</sub> ( $\text{mol O}_3 \text{ m}^{-2} \text{ s}^{-1}$ ) in Web-D O<sub>3</sub>SE .**

Parameter	Web-DO <sub>3</sub> SE	ZHANG	CMAQ_J	TEMIR	NOAH-GEM	CMAQ_p
<b>G<sub>max</sub> or V<sub>Cmax</sub></b>	$g_{max}$ [ $\text{cm s}^{-1}$ ]	$g_{max}$ [ $\text{cm s}^{-1}$ ]	$g_{max}$ [ $\text{cm s}^{-1}$ ]	$V_{Cmax}^+$ [ $\mu\text{mol CO}_2 \text{ m}^{-2} \text{ s}^{-1}$ ]	$V_{Cmax}$ [ $\mu\text{mol CO}_2 \text{ m}^{-2} \text{ s}^{-1}$ ]	$V_{Cmax}$ [ $\mu\text{mol CO}_2 \text{ m}^{-2} \text{ s}^{-1}$ ]
Forests	0.44 (EN) 0.49 (EB) 0.55 (DB)	0.25 (EN) 0.42 (EB) 0.42 (DB)  Zhang et al., 2003	0.36 (EN), 0.53 (EB), 0.32 (DB),  Pleim & Ran, 2011	60.1 (EN) 59.0 (EB) 55.4 (DB),  (Oleson et al, 2013; NCAR Technical	57.6 (EN) 96 (EB) 96 (DB)  Niyogi et al., 2009; JAMC	57.6 (EN, Slevin et al 2015), 49.2 (EB, Medi. forest, (EB_tr+EB_te)/2,Oliv



				notes)		er et al., 2022), 55.4 (DB, CLM4.5, Kattge 2009)
Crops	1.1 (wheat) 0.74 (maize) 0.73 (soybean)	0.53	0.91	96.7	76.8	96.7 (CLM4.5)
Grasses	0.66	0.64	0.64	75.1	28.8	75.1 (CLM4.5)

202

203  $POD_y$  is calculated in post-processing, according to the guidelines in UNECE LRTAP (2017):.

204 
$$POD_y = \sum_{i=1}^n [fst, sun_i - y] * \left( \frac{3600}{10^6} \right) \quad \text{for } fst, sun_i \geq y \text{ nmol m}^{-2} \text{ PLA s}^{-1}$$

205 Where  $fst, sun_i$  is the hourly mean  $O_3$  flux in  $\text{nmol } O_3 \text{ m}^{-2} \text{ PLA s}^{-1}$  at sunlit leaves,  $y$  is a species-dependent  
206 threshold (crops:  $6 \text{ nmol } O_3 \text{ m}^{-2} \text{ s}^{-1}$ , grassland and forests:  $1 \text{ nmol } O_3 \text{ m}^{-2} \text{ s}^{-1}$ ; UNECE LRTAP (2017) and  $i$  is the  
207 number of daylight hours (when  $ssrd > 50 \text{ W m}^{-2}$ ) within the accumulation period (growing season). The term  
208  $(3600/10^6)$  converts from  $\text{nmol m}^{-2} \text{ PLA s}^{-1}$  to  $\text{mmol } O_3 \text{ m}^{-2} \text{ PLA}$ .  $fst, sun$  is calculated by:

209 
$$f_{st, sun} = c \frac{(z) * g_{st} * r_c}{r_b + r_c}$$

210 Where  $c(z)$  is the  $O_3$  concentration at in  $\text{nmol m}^{-3}$  (calculated from ppb by multiplying by  $P/RT$  where  $P$  is the  
211 atmospheric pressure (Pa) and  $T$  is the air temperature (K)



212 ,  $R$  is the universal gas constant of  $8.31447 \text{ J mol}^{-1} \text{ K}^{-1}$  and  $T$  is the assumed standard air temperature (293 K).  
 213 The leaf surface resistance ( $r_c$ ) is given by  $r_c = 1/(g_{st} + g_{ext})$  where  $g_{ext}$  is the inverse of cuticular resistance.  
 214 . The leaf boundary resistance is calculated by:

$$215 \quad r_b = 1.3 * 150 * \sqrt{\frac{L}{u(h)}}$$

216 Where factor 1.3 accounts for the differences in diffusivity between heat and  $O_3$ ,  $L$  is the crosswind leaf  
 217 dimension (i.e. leaf width in m) and  $u(h)$  is the wind speed at the top of the canopy.

## 218 **2.4 Description of stomatal deposition model simulations**

219 The result section aims at identifying trends in stomatal deposition models among different land cover types  
 220 including grass, crops and forests using four model experiments as follows.

221 **In experiment 1**, the different models are driven by the  $O_3$  and meteorological data from ERA5. We analysed  
 222 the simulated deposition velocity ( $V_d$ ) split into stomatal and non-stomatal fractions, canopy ( $G_{st}$ ) and sunlit  
 223 ( $G_{sun}$ ) stomatal conductance.

224 To include observational constraints, in **experiment 2**, the TEMIR, ZHANG, NOAH, MESSy and CMAQ  
 225 models were run with data obtained from the FLUXNET database (available for three sites, see Table 1), and the  
 226 simulated  $G_{st}$  was evaluated with observation-derived values, inferred  $G_{st}$ , of SynFlux. Spearman correlation was  
 227 applied for the model evaluation, as it can be applied to any datasets including non-parametric and non-linear  
 228 ones. The US-Ha1 and FI-Hyy sites were considered for the model evaluation due to the availability of SynFlux  
 229 data at these sites

230 A sensitivity analysis (**experiment 3**) was performed by driving a set of models with synthetic input data in the  
 231 following steps: i.  $O_3$  input was perturbed by  $\pm 40\%$  (Sofen et al. 2016). ii. soil water content was perturbed by  
 232  $\pm 30\%$  (Li et al., 2020). iii. absolute humidity was perturbed by  $\pm 30\%$ , soil and air temperatures were  
 233 perturbed by  $\pm 3$ , independently, iv. the growing season, which was mostly approximated by LAI, was shifted  
 234 by 14 days forward and backward in time. In set (iii) and (iv), relative humidity was calculated from absolute





humidity and temperature after their perturbation. In both cases, absolute humidity was capped at the saturation vapour pressure at the corresponding temperature.

Finally, for **experiment 4**,  $g_{\max}$  and  $V_{C\max}$  of the models were varied by  $\pm 20\%$ , based on previous estimates of plant traits dependent uncertainty (e.g., Walker et al., 2017; UNECE LRTAP, 2017).

### 3. Results

#### 3.1 General characteristics of simulated total deposition velocity and stomatal contribution

The split of total  $O_3$  deposition between different pathways,  $G_{st}$ ,  $G_{cut}$ ,  $G_{ground}$ , simulated by the 7 models is shown for each of the 9 sites in Figure 2 (corresponding data are presented in Table S9). This analysis allows us to briefly assess the overall efficacy of the model's ability to simulate deposition velocity  $V_d$  (by comparisons with previously published values; more complete assessments of model's ability for some of these sites can be found in Clifton et al., 2023) and to compare the importance of the stomatal deposition pathway between models for different land cover types and across different seasons.

Observations of  $V_d$  have only been made at a handful of sites i.e. Hyytiälä, Finland; Castelporziano, Italy; Grignon, France and Harvard Forest, US (close to our Quabbin site in terms of proximity, land cover type and climate). Overall, the models capture  $V_d$  at these sites compared to observed values reported in previous studies. Namely, the observed seasonal cycle in  $V_d$  at Hyytiälä, Finland (needleleaf forest), with lows of  $\sim 0.1 \text{ cm s}^{-1}$  between January and April and highs of  $0.4 \text{ cm s}^{-1}$  between June to September, averaged over 10 years of measurements from Clifton et al. (2023) and Visser et al. (2021) are captured by most models except of MESSy and TEMIR, which reach  $V_d$  values of  $0.8 \text{ cm s}^{-1}$  during the summer. Similarly, the strong seasonal cycle in  $V_d$  at Quabbin, US (temperate mixed forest), ranging from around  $0.2 \text{ cm s}^{-1}$  between January and April up to  $0.5 \text{ cm s}^{-1}$  from June to September in Clifton et al. (2023) is captured by all models. Observed  $V_d$  at Castelporziano, Italy (evergreen broadleaf forest) shows relatively constant values throughout the year, commonly between  $0.4$  and  $0.8 \text{ cm s}^{-1}$  averaged over a 2-year period (Savi & Fares, 2014). The study by Stella et al. (2011) reports  $V_d$  measurements of  $0.63 \text{ cm s}^{-1}$  (on average) at Grignon (France). At the other sites, no  $O_3$  dry deposition measurement exists and thus we report the observed ranges for the land cover type (and possibly the matching climate). Over grassland, Silva and Heald (2018, and references therein) show a mean of 11 measurements of daytime  $V_d$  values ( $\sim 0.4 \text{ cm s}^{-1}$ ) in agreement with our models. Measurements exist at soybeans and maize crops



which indicate  $V_d$  values of 0.7 (Meyers et al., 1995) and 0.4 - 0.6 cm s<sup>-1</sup> (Stella et al., 2011), respectively. Thus, the models seem to estimate too low deposition at soybeans.

In terms of deposition pathways, for all sites and models, stomatal deposition consistently ranks as the most important pathway in the summer, whereas in winter and, for some models, in the fall  $G_{st}$  decreases to zero to very low at sites with seasonal variation in vegetation coverage. The importance of the pathway varies with land cover type and season. The highest stomatal contribution of 90 % (NOAH model) is shown at the Amberd site. Among the different land cover types, the highest average stomatal contribution to deposition during the summer is estimated across grass (67 %), followed by crops (65 %) and forests (59 %). The seasonal importance of stomatal contribution is not seen for the tropical sites as the year- round growing season means that stomatal conductance is driven by solar radiation which is constant throughout the year (e.g. Hardacre et al., 2015). Previous studies involving measurements and partitioning approaches (Horvath et al., 2018, Meszaros et al., 2009) indicate that the non-stomatal  $O_3$  deposition pathways (i.e.,  $G_{ground}$  and  $G_{cut}$ ) are very strong (in some cases, dominant over  $G_{st}$ ) at short vegetation such as the grasslands. Despite there are multiple factors such as wind speed, solar radiation, LAI, etc., that control the relative contributions of the three deposition branches,  $G_{st}$  is the dominant pathway at the three grassland sites of the current study (Amberd, Mt Kenya, and Peru). At the Amberd and Perus sites,  $G_{cut}$  and  $G_{ground}$  are low due to lower wind speeds (e.g., at the Peru Site in the Summer season, the mean wind speed was 1.0 cm s<sup>-1</sup> and the  $G_{cut}$  and  $G_{ground}$  contributions in the TEMIR model were 21 % and 12 %, respectively; Table S3).

In contrast, at the Mt Kenya site,  $G_{st}$  overcomes the  $G_{cut}$  and  $G_{ground}$  due to higher solar radiation at this site (annual mean is 246 W m<sup>-2</sup>, Table S2). Therefore, it can be inferred that the  $O_3$  deposition pathway depends on not only the land cover type but also meteorological drivers. Among the models, Web-DO<sub>3</sub>SE estimated the lowest stomatal contribution at grass (Fig. 2) most likely due to its parallel pathways to cuticle, soil and stomata, with the former scaled by LAI with a constant cuticular deposition of 2500 s m<sup>-1</sup>. Such differences in model structures likely led to the wide-ranging partitioning. For example, for the Quabbin site (summer), all models simulate  $G_{cut}$  ranging from 15-65 %,  $G_{ground}$  from 2-19 % and  $G_{st}$  from 33-66 % despite their agreement on the overall  $V_d$  values (total bar). Models agree better in the partitioning of  $O_3$  dry deposition to crops with summer stomatal fraction contributions ranging between 46-73 %, 37-73 % and 51-81 % for US-Ne3 Maize, US-Ne3 soybeans and FR-Gri (rapeseed and wheat). Most models estimate non-stomatal deposition equal to or larger than the stomatal contribution to deposition outside of the tropics in winter and fall, and to some extent in spring. This again emphasises the importance of the stomatal contribution to the seasonal cycle of total deposition as



292 also found in Clifton et al. (2023). Similarly, as seen at grasslands, Web-DO<sub>3</sub>SE (Fig. 2, Table S3) accounts for  
293 the highest non-stomatal deposition at crop sites.  
294 Across all forest sites, models show significant cuticular uptake throughout the year ranging between 11 % and  
295 94 % contribution. At FI-Hyy,  $G_{\text{cut}}$  averages ~50 % across all seasons and all models with higher estimates of  
296 ~55 % by the TEMIR model due to the higher wind speed at FI-Hyy (annual mean wind speed is 3.2 m s<sup>-1</sup>; Table  
297 S2) favoring cuticular deposition as suggested by Rannik et al. (2012). At IT-Cpz, our models estimate on average  
298 around 43 % (20-80 %) to be non-stomatal deposition, close to the previously reported ranges (Gerosa et al. 2005,  
299 Fares et al. 2012, Fares et al. 2014), which were up to 57 % from non-stomatal deposition and 30-60 % from  
300 stomatal uptake. A similar partitioning (59 %  $G_{\text{st}}$ , 33 %  $G_{\text{cut}}$ , 5 %  $G_{\text{ground}}$  model average in summer) is seen at  
301 PhaDin.





**Fig. 2 Seasonal mean effective conductances of the cuticular ( $G_{\text{cut}}$ ), ground ( $G_{\text{ground}}$ ), and stomatal ( $G_{\text{st}}$ ) deposition pathways of  $\text{O}_3$  across various models and sites (Exp#1).**

All models except Web- $\text{DO}_3$  SE were compared on a seasonal and hourly basis with the SynFlux  $G_{\text{st}}$  data for US-Ha1 and FI-Hyy sites (Figures S2, S3). CMAQ\_J, NOAH, TEMIR, and ZHANG show reasonable agreement at the Quabbin forest (US-Ha1) whereas CMAQ\_P and MESSy show quite significant overestimates at both FI-Hyy and Harvard Forest (Table S4) and CMAQ\_J overestimates at FI-Hyy only. Note that NOAH and ZHANG show significant underestimates at FI-Hyy while agreeing well with SynFlux at Harvard Forest (Quabbin). The underestimates by the ZHANG model are consistent with the results from a similar comparison for Yellowstone National Park in the US by Mao et al. (2024). Compared to Harvard Forest, FI-Hyy is the most humid and cloudy with the lowest solar radiation flux, and these conditions likely contribute to the underestimates by the NOAH and the ZHANG model as identified by Mao et al. (2024). The differences between modelled and SynFlux  $G_{\text{st}}$  do not seem to be associated with the model types, i.e. empirical or photosynthesis-based models.

The correlation of the diurnal cycle of  $G_{\text{st}}$  calculated by the models with the inferred  $G_{\text{st}}$  by SynFlux for US-Ha1 and FI-Hyy (Fig. S4) confirms that models generally capture the temporal patterns of  $G_{\text{st}}$  of at least these two different forest types and climates (FI-Hyy: EN, temperate, subarctic; Quabbin: DB, moist temperate). The best Spearman correlations are found at FI-Hyy and range between 0.73 by the MESSy model and 0.85 by the TEMIR model. Overall lower correlations are found at the Quabbin site ranging from 0.65 for the NOAH and MESSy models to 0.82 for the CMAQ\_P model. This poorer correlation suggests that additional water stress may limit stomatal conductance at Quabbin, which the models do not capture, compared to FI-Hyy. Notably, a similar range of correlation coefficients (0.61 – 0.93) was found when modelled  $G_{\text{st}}$  values obtained using the TOAR input data were compared with SynFlux  $G_{\text{st}}$ . As SynFlux data were generated using FLUXNET measurement data, this result corroborates the validity of using the TOAR database as input to Web- $\text{DO}_3$ SE, developed as a service website to aid in risk assessment of  $\text{O}_3$  damage to European vegetation.

To identify the key drivers of the  $G_{\text{st}}$  model schemes among different land cover types and climate conditions, we also compare estimates of  $G_{\text{st}}$  between models for all sites and analyse the similarity of  $G_{\text{st}}$  diurnal cycles in empirical and photosynthesis models. The average diurnal variations of stomatal conductance ( $G_{\text{st}}$ ) of  $\text{O}_3$  at the



9 sites for each season are shown in Figure 3. This also helps interpret the modelled stomatal conductance of sunlit leaves ( $G_{\text{sun}}$ ) shown in Fig 4. Across all models, the diurnal mean  $G_{\text{st}}$  (Fig. 3) varied from  $0.15 \text{ cm s}^{-1}$  (Quabbin) to  $0.50 \text{ cm s}^{-1}$  (Mt. Kenya). In the TEMIR and the ZHANG model, roughly 50% of  $G_{\text{st}}$  occurs at the sunlit part of the leaves. Web-DO<sub>3</sub>SE and CMAQ\_P  $G_{\text{sun}}$  contribute 30 % on average (Fig. 4). At mid-to-high latitudes, the model spread is limited to the summer season, whereas at tropical sites, it is similar throughout the year. During the day, models show a spread of  $1.2 \text{ cm s}^{-1}$  in  $G_{\text{st}}$  at the forest and grassland sites during the summer while their predictions agree most at the crop sites (throughout the year) with a maximum of  $1.0 \text{ cm s}^{-1}$ . This is due to the flux response relationship which has a more sensitive response (steeper slope for most crops) due to a higher threshold (see Table 5 for the equations describing the steepness of the change). Results among the same model type differed significantly while different model types could produce similar results at the same location. For the sites with distinct seasonal variations, model differences were the largest in summer.

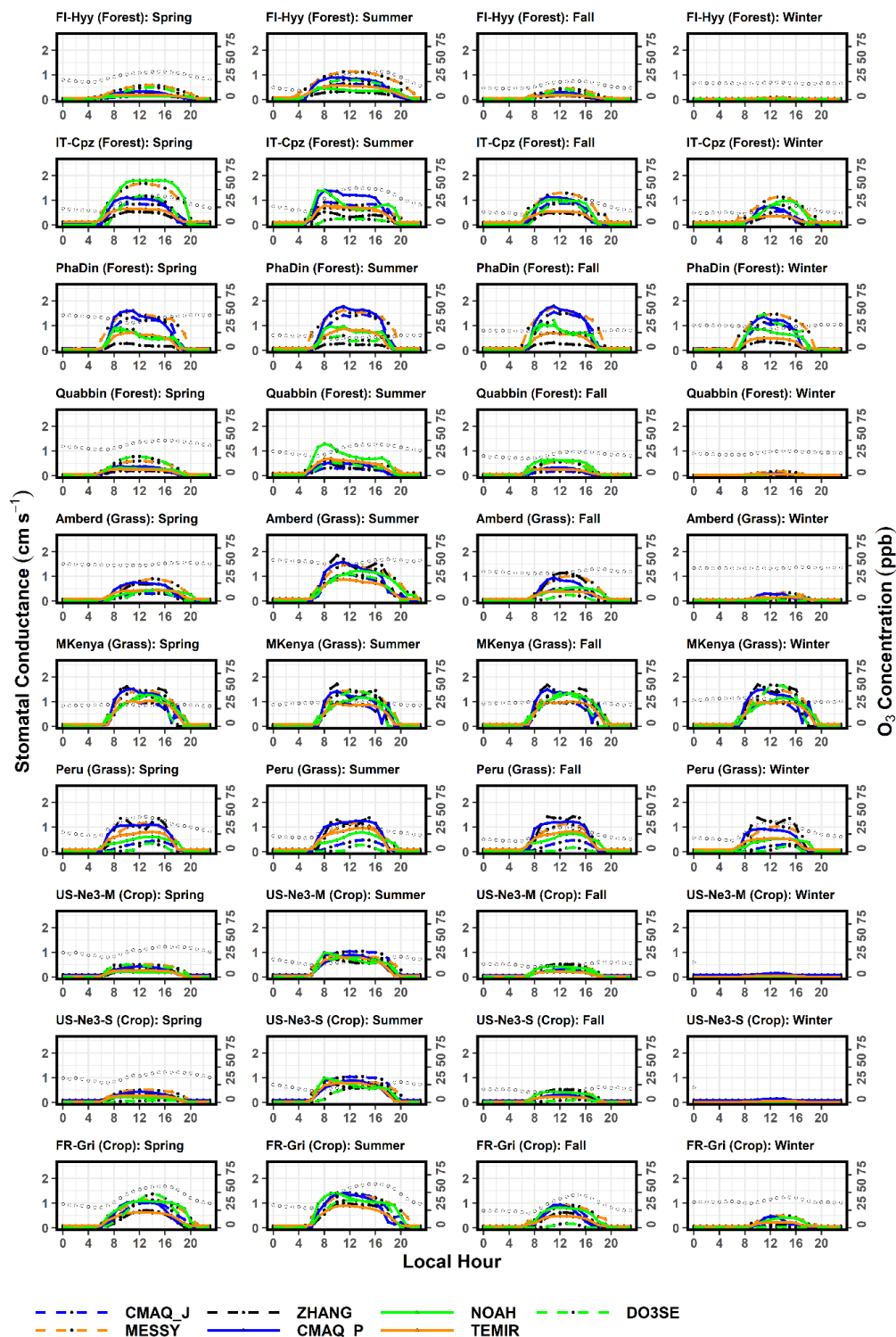
In comparison, TEMIR and ZHANG, photosynthesis-based and Jarvis-style, respectively, are both governed mainly by solar radiation (see higher  $G_{\text{sun}}$  in Fig. 4), showing close agreement, except in summer, at the forest sites (ZHANG values are very low). Only these two show a midday depression in  $G_{\text{sun}}$  at the peak of solar radiation at Mt Kenya (the site with the highest radiation). The ZHANG model also estimated this feature for  $G_{\text{sun}}$  and  $G_{\text{st}}$  at other grassland sites (Fig. 3 and 4). This feature could be due to the day length (seasonality) scaling of  $V_{\text{Cmax}}$  in TEMIR, causing  $G_{\text{st}}$  to increase significantly during summer at higher latitude sites. In contrast, at lower latitude sites (Mt Kenya and Huancayo, Peru), the seasonal variation in day length is smaller and subsequently smaller seasonality in  $V_{\text{Cmax}}$  and  $G_{\text{st}}$ . The TEMIR and the CMAQ\_P models, both photosynthesis-based, estimate very similar  $G_{\text{sun}}$  values (Fig. 4) at PhaDin (fall, winter), IT-Cpz (spring, summer) and FI-Hyy (summer) whereas the  $G_{\text{st}}$  estimates show significant differences. The opposite occurs at Quabbin where the  $G_{\text{sun}}$  values of the two models differ much more than the  $G_{\text{st}}$  estimates. These results illustrate that the different fractionations between shaded and sunlit leaves could mainly contribute to the model spread in stomatal conductance.

Further examination of individual models' features can shed light on the causes of model/site differences in  $G_{\text{st}}$ . The MESSy  $G_{\text{st}}$  value is strongly governed by LAI followed by soil moisture, and in all other respects MESSy treats different land cover types the same. Therefore, MESSy simulates the highest  $G_{\text{st}}$  values at PhaDin, Grignon and Mt. Kenya with LAI values of 6.9, 4.3 and  $4.2 \text{ m}^2 \text{ m}^{-2}$ , respectively (Table 1). In contrast to PhaDin, the high LAI site IT-Cpz ( $6.9 \text{ m}^2 \text{ m}^{-2}$ ) experiences significant water stress during summer. This is only captured by MESSy and NOAH indicating higher sensitivity to water stress. During the day, an evident midday



depression of  $G_{st}$  due to hot weather and water shortage is seen accompanied by a peak in the early morning evident from NOAH, same as has been observed in Mediterranean ecosystems (e.g. Gerosa et al. 2005). The NOAH model accounts for the direct effect of relative humidity on  $G_{st}$  (see model description in the supplement) and subsequently modelled a depression in  $G_{st}$  at the daily onset (8 am). This variation explains the  $G_{st}$  peak at IT-Cpz and Quabbin, which are especially in the summer the two driest among all sites. Due to the dry conditions at the Quabbin site, low soil water and relative humidity, most models, except NOAH, simulate the lowest summer daily mean  $G_{st}$  values among all sites. The high estimate by the NOAH model can be explained by the highest  $V_{C_{max}}$  value among the photosynthesis models (Table 4). The high  $g_{max}$  value of  $0.55 \text{ cm s}^{-1}$  used in Web-DO<sub>3</sub>SE leading to large estimates is largely dampened by strong soil moisture stress at IT-Cpz (Table S2). Similarly, Web-DO<sub>3</sub>SE estimates the lowest  $G_{st}$  (among the models) values at the Peru site (grassland) due to a strong limitation by the  $f_{temp}$  function on stomatal conductance suggesting that the minimum temperature for stomatal opening at  $12^\circ\text{C}$  is too low for these cool temperate conditions. The ZHANG estimates are generally governed by  $g_{max}$ , explaining the highest and lowest  $G_{st}$  values of all models simulated with the ZHANG model at grassland and forest sites, respectively. The CMAQ\_J model has the lowest  $g_{max}$  values, but it is strongly impacted by soil moisture. The additional dependence of the ZHANG model on solar radiation is reflected in higher  $G_{sun}$  relative to  $G_{st}$  (Fig. 3 and 4). TEMIR also simulates the smallest spread of  $G_{st}$  among the 3 grassland sites (Ambred, MKenya, Peru), as temperature acclimation of photosynthesis (Kattage and Knorr, 2007) is implemented. The different temperatures among the 3 sites have smaller effects on photosynthetic capacity and  $G_{st}$  than other models. Despite explicitly considering soil water stress, TEMIR does not capture the impacts of water stress on  $G_{st}$  in IT-Cpz and Quabbin in the summer, as the equivalent soil moisture threshold to trigger soil water stress at IT-Cpz and Quabbin is very low ( $<0.1 \text{ m}^3 \text{ m}^{-3}$ ). Both versions of CMAQ respond very strongly to soil moisture which may not be accurate for each site. The differences between CMAQ-J and CMAQ-P are greatest at the sites with the greatest LAI, such as IT-Cpz and PhaDin.

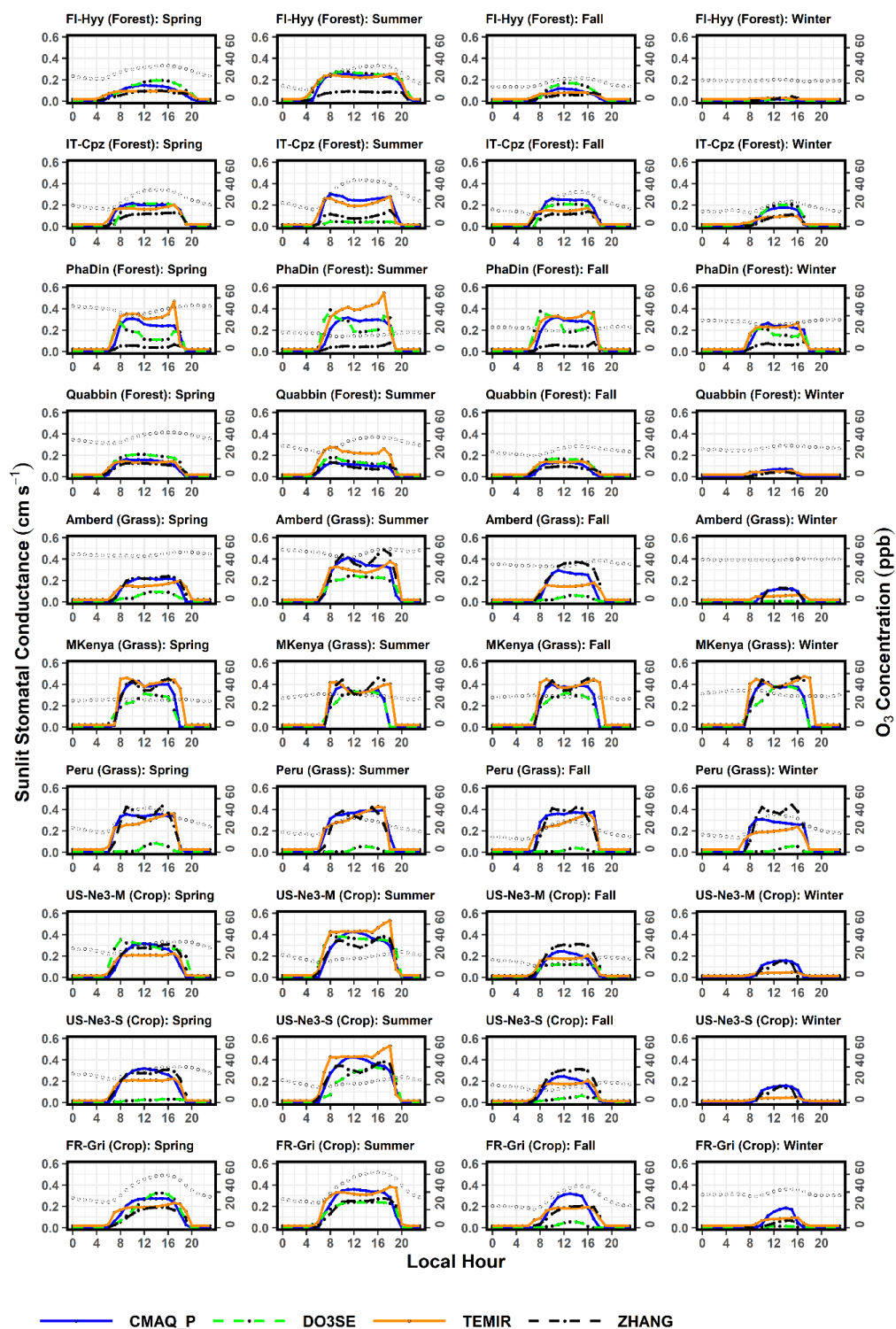








385 **Fig. 3 Multi-year diurnal cycle of growing season  $G_{st}$  from models at 9 different sites. Four topmost panels**  
386 **are the forest sites, three panels in the middle are grass sites, and three lowermost panels are crop sites.**  
387 **Open circles indicate diurnal  $O_3$  variations**





389 **Fig 4 Leaf level sunlit stomatal conductance ( $G_{\text{sun}}$ ) from the 3 two-leaf models (CMAQ\_P, TEMIR, and**  
 390 **ZHANG) at 9 different sites. Four topmost panels are the forest sites, three panels in the middle are grass**  
 391 **sites, and two lowermost panels are crop sites (US-Ne3-S=soybeans, US-Ne3-M=maize). Open circles**  
 392 **indicate diurnal  $O_3$  variations**

393 The difference between total and sunlit stomatal flux is examined, and trends of stomatal sunlit flux are  
 394 characterized by different land cover types and climate conditions. Figures 5 and 6 show the ( $\text{SRAD} > 50 \text{ W m}^{-2}$ )  
 395 stomatal  $O_3$  flux ( $F_{\text{st}}$ ) and stomatal, sunlit  $O_3$  flux ( $F_{\text{st,sun}}$ ) for different models per season at 9 sites representing  
 396 forest (top), grass (middle), crops (bottom). Thereby, we consider whether  $G_{\text{st}}$  and  $O_3$  concentration co-vary at  
 397 diurnal and seasonal timescales. Across all land cover types, a large range of  $F_{\text{st}}$  ( $0.05\text{--}2 \text{ ppb m s}^{-1}$ , Fig. 5) is  
 398 estimated, usually highest in spring and summer and lowest in winter. The largest median of  $F_{\text{st}}$  is found at  
 399 Amberd ( $0.75 \text{ ppb m s}^{-1}$ ; ZHANG, summer), followed by IT-Cpz ( $0.60 \text{ ppb m s}^{-1}$ ; NOAH, spring), and FR-Gri  
 400 ( $0.60 \text{ ppb m s}^{-1}$ ; MESSy and NOAH, summer) owing to both higher  $G_{\text{st}}$  and  $O_3$  concentrations at the respective  
 401 sites (Fig. 3). Consequently, no general trend can be identified among the sites, i.e. flux estimates can differ  
 402 within one land cover type. Namely, the two crop sites show very different  $F_{\text{st}}$  estimates (Fig. 5) since they have  
 403 the most different  $O_3$  levels across one land cover type. While the FR-Gri site is exposed to an annual mean  $O_3$   
 404 of 45 ppb (Table S1) as the lowest  $O_3$  level of 25 ppb among all sites. The same applies for the diurnal variation  
 405 of  $O_3$  causing either a high (FR-Gri) or a low range (US-Ne3) of flux estimates among all models (in summer  
 406 and spring). The difference is less apparent in the  $F_{\text{st,sun}}$  estimates (Fig. 6) which point to the sensitivity of the  
 407 two leaves to  $O_3$  concentration. Similarly, as seen for the stomatal conductance, three of four models show a  
 408 very good agreement of  $F_{\text{st}}$  and  $F_{\text{st,sun}}$  among each other. In terms of seasonality, models agree also generally  
 409 well among the grassland sites. Among those (and all land cover types), the maximum annual median  $F_{\text{st,sun}}$  was  
 410 estimated for Amberd attributed to the high daytime (7 am - 7 pm) annual  $O_3$  concentrations (49.3 ppb, Table  
 411 S1). The most different  $F_{\text{st,sun}}$  (and  $F_{\text{st}}$ ) values are found between the ZHANG (highest) and Web-DO<sub>3</sub>SE  
 412 model (lowest) due to the difference in  $G_{\text{sun}}$  (Fig. 4). Web-DO<sub>3</sub>SE disagrees the most with the other models and  
 413 predicts very small fluxes at the Peru site following the small  $G_{\text{st}}$  and  $G_{\text{sun}}$  values (Fig. 3 and 4).

414 Among forest sites, spring  $F_{\text{st,sun}}$  values are comparably high as summer fluxes following the seasonal variation  
 415 of  $G_{\text{sun}}$  (Fig. 6, outside the tropics). The highest spring estimates at PhaDin and Quabbin (forests) are linked to  
 416 the site-specific yearly  $O_3$  maximum in this season (Fig. 3). The flux seasonal maximum is more pronounced in  
 417 all four models (ZHANG, CMAQ\_P, TEMIR) when the  $O_3$  concentration variation during the year is larger at  
 418 the respective site. The highest  $F_{\text{st,sun}}$  ( $0.1 \text{ ppb m s}^{-1}$ ) is estimated by TEMIR at PhaDin (spring) reflecting the



high  $G_{\text{sun}}$  estimate. In contrast, when considering the total  $F_{\text{st}}$ , CMAQ\_P shows the highest estimate (Fig. 5) which indicates that TEMIR uses a higher sunlit fraction than CMAQ\_P as it has been shown for stomatal conductance (Fig. 3 and 4). The difference is most apparent at high LAI sites (PhaDin, IT-Cpz, FR-Gri). The lowest estimates of  $F_{\text{st,sun}}$  (and a very small spread) at the forest sites are shown by the ZHANG model as it has been explained for  $G_{\text{st}}$  and  $G_{\text{sun}}$ . Overall, CMAQ\_P has the lowest spread among the models which was also found in the multi-model comparison study by Clifton et al. (2023).

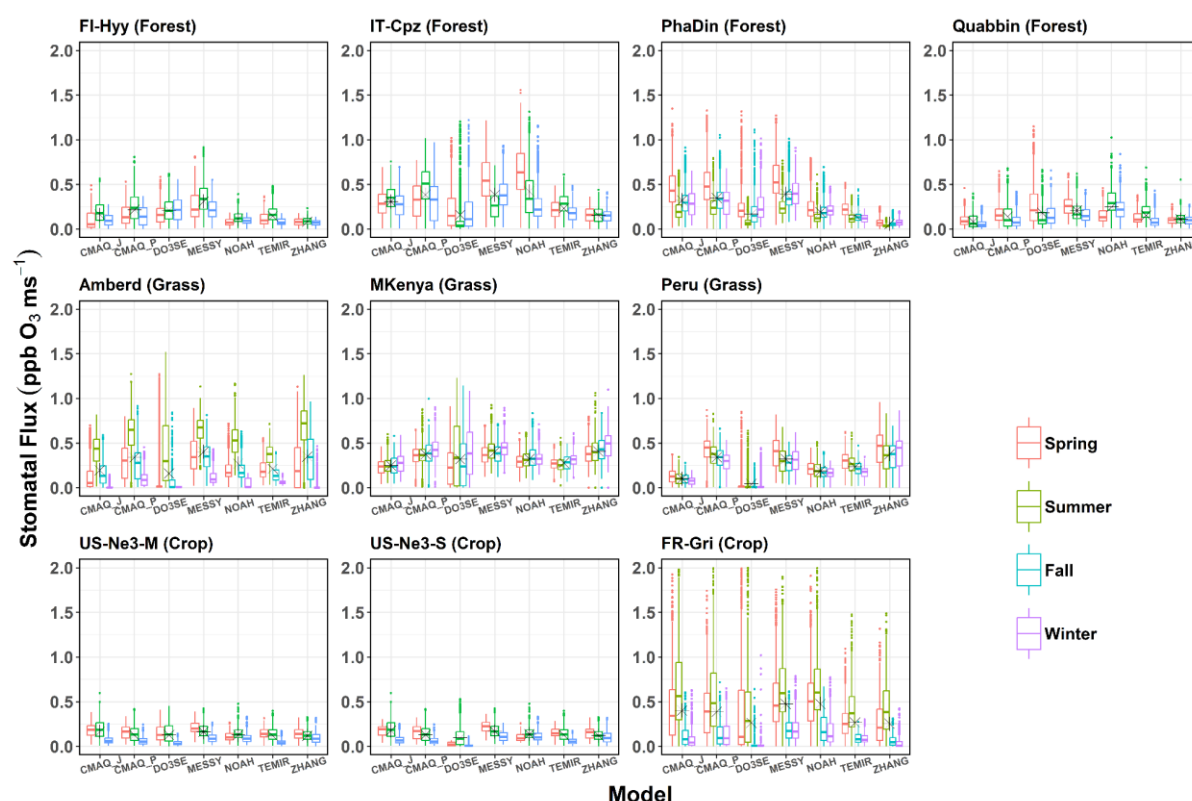


**Fig 5: Boxplots of seasonal mean canopy-level total stomatal  $O_3$  flux ( $\text{ppb ms}^{-1}$ ) for different models at the different 9 sites (data represent  $\text{SRAD} > 50 \text{ W m}^{-2}$  and the growing period).**

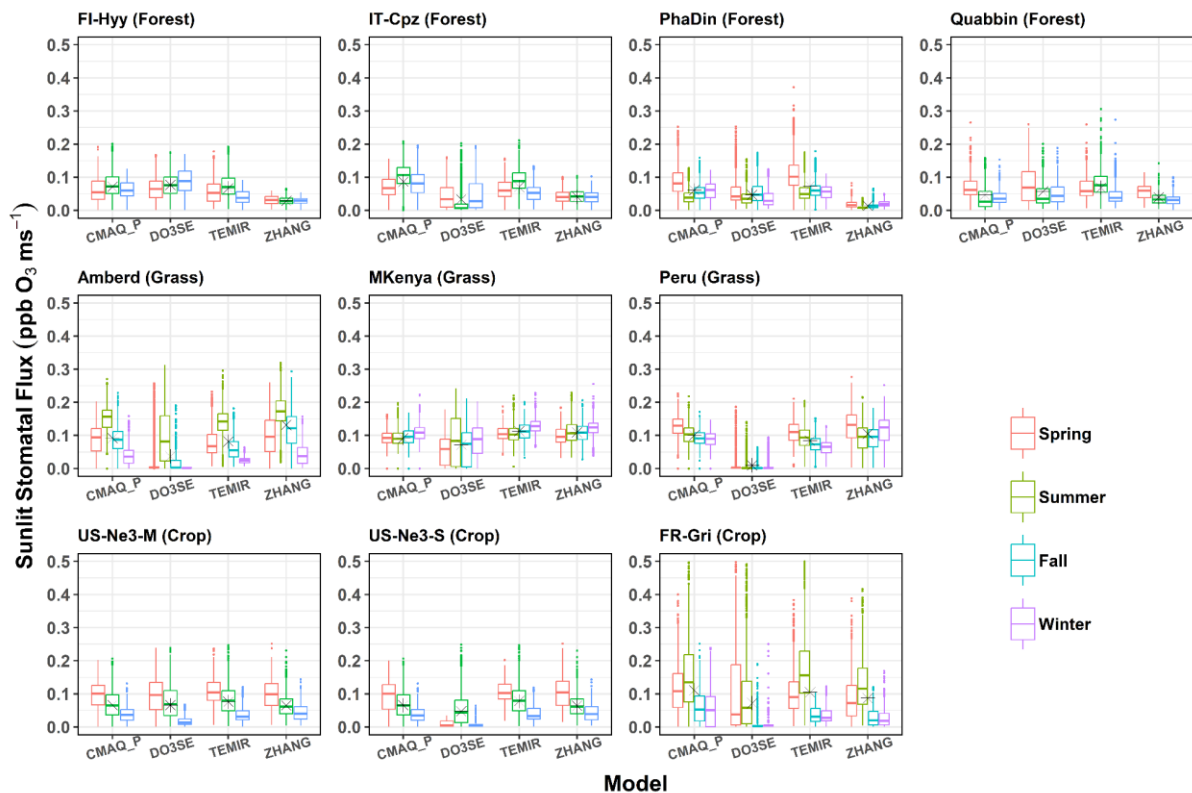


**Fig 6: Boxplots of seasonal mean leaf-level sunlit stomatal  $O_3$  flux ( $ppb\ ms^{-1}$ ) for different models at the different 9 sites (data represent  $SRAD > 50\ W\ m^{-2}$  and the growing period).**

### 3.2 Vegetation impact and variation with key input data

This section presents the  $POD_y$  calculated from the  $O_3$  deposition by different models at 9 different stations to identify trends and patterns of  $POD_y$  among land cover types and climates (Fig. 7, corresponding data in Table S9). By driving the models with changed input data of  $O_3$ , soil moisture, temperature, relative humidity, growing season (Fig. 8) and with changed  $V_{c_{max}}/g_{max}$  parameter (Fig. 9) we explore the sensitivity of the  $POD_y$  estimates. As shown in the previous analysis, the largest  $O_3$  uptake and thus the highest  $POD_y$  of  $28\ mmol\ O_3\ m^{-2}$  (on average among all models) is estimated over grassland sites (compared to forest and crops) (Fig. 7).  $POD_1$  increases linearly with time for evergreen grasslands whereas Mt. Kenya shows the fastest accumulation (due to



the highest  $F_{st}$  in spring and summer). Three of the four models lie in a range of  $5 \text{ mmol O}_3 \text{ m}^{-2}$  whereas Web-DO<sub>3</sub>SE predicts a maximum  $POD_y$  of  $10 \text{ mmol O}_3 \text{ m}^{-2}$  at all grassland sites. Only at the Peru site, these low values can be reasoned by the significantly lower  $G_{ssun}$  and  $F_{st,sun}$  (compared to other models).

For forests, our modelled ensemble  $POD_1$  median and maximum values (ranging between  $8$  and  $25 \text{ mmol O}_3 \text{ m}^{-2}$ ) are similar in scale to values estimated across broad geographical regions by other studies. Karlsson et al. estimated  $POD_1$  values across Europe with the highest values in mid-latitude Europe for coniferous ( $15$  to  $20 \text{ mmol O}_3 \text{ m}^{-2}$ ) and broadleaf ( $22$  to  $28 \text{ mmol O}_3 \text{ m}^{-2}$ ) forests. However, the ZHANG and the Web-DO<sub>3</sub>SE model are estimated to be significantly lower  $POD_1$  than CMAQ\_P and TEMIR at each site. These estimates average to  $16 \text{ mmol O}_3 \text{ m}^{-2}$ . There is no obvious pattern to which models tend to estimate higher or lower  $POD_1$  values, but these estimates are generally consistent with  $G_{sun}$  (Fig. 4) and  $F_{st,sun}$  (Fig. 6) model estimates explained by particular model constructs or parameterisations. For instance, the ZHANG model estimates low stomatal deposition and thus also  $POD_y$  over all forests. Web-DO<sub>3</sub>SE saw a low  $O_3$  uptake only due to the site conditions at IT-Cpz.

For crops, the model estimates of  $POD_6$  are a little more consistent, with modelled differences within sites only varying between  $\sim 3$  and  $11 \text{ mmol O}_3 \text{ m}^{-2}$ , however, this could in part be due to the overall lower  $POD_6$  values due to the use of the higher  $y$  threshold. Median model ensemble values range between  $\sim 7$  and  $12 \text{ mmol O}_3 \text{ m}^{-2}$  across sites.  $POD_6$  for staple crops has been estimated in other studies across Europe and globally. A European study (Schucht et al., 2020) on wheat found  $POD_6$  values up to  $\sim 4 \text{ mmol O}_3 \text{ m}^{-2}$  suggesting that our  $POD_6$  values for the FR-Gri site tend to be too high. Feng et al. (2012) estimated maximum  $POD_6$  values of up to  $8 \text{ mmol O}_3 \text{ m}^{-2}$  for winter wheat in China though these higher values are likely driven by higher ozone concentrations. Similarly, Wang et al. (2022) also found  $POD_6$  values for maize of up to  $8 \text{ mmol O}_3 \text{ m}^{-2}$ . Our models give the largest range in  $POD_6$  estimates for soybeans at the US-Ne3 site ( $0$  to  $11 \text{ mmol O}_3 \text{ m}^{-2}$ ). A key determinant of the range in  $POD_y$  simulated by our models, and also with estimates provided in the literature, is the value chosen for  $g_{max}$  (or  $V_{Cmax}$  depending on the model construct). For example, the multiplicative  $g_{sto}$  models used to derive flux-response relationships (see Table 5) use  $g_{max}$  values of  $450$ ,  $126$  and  $301 \text{ mmol O}_3 \text{ m}^{-2} \text{ s}^{-1}$  for wheat, maize and soybeans (UNECE LRTAP, 2017; Peng et al., 2019 and Zhang et al., 2017). By contrast, our modelling uses a variety of  $g_{max}$  values, for example, the Web-DO<sub>3</sub>SE model uses  $450$ ,  $305$  and  $300 \text{ mmol O}_3 \text{ m}^{-2} \text{ s}^{-1}$  for wheat, maize and soybeans. A further consideration in parameter selection are local conditions, a study by Stella et al., (2013) found a  $g_{max}$  value of  $296 \text{ mmol O}_3 \text{ m}^{-2} \text{ s}^{-1}$  was most appropriate to describe wheat  $g_{sto}$  at the FR-Gri site. This variation highlights the importance of selecting appropriate model



parameterisation for conditions, as well as consistency of parameterisation with models used to develop flux response relationships.

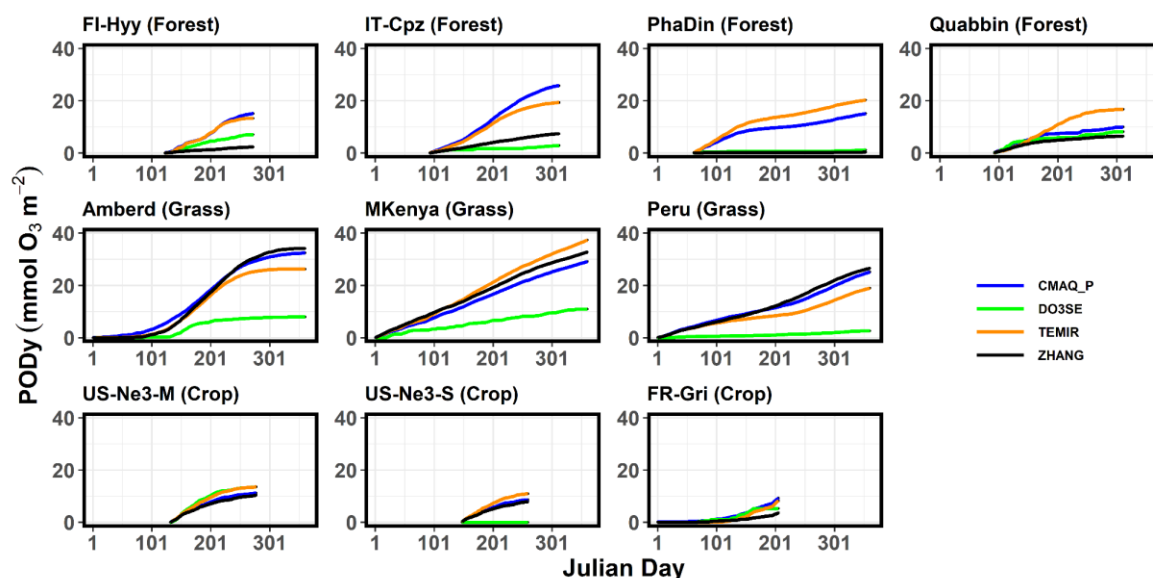


**Fig 7: Evolution of  $POD_y$  ( $mmol\ O_3\ m^{-2}$ ) through the growing seasons at various sites.**

From the sensitivity analysis, we found that all models show sensitivity of  $POD_y$  to changes in  $O_3$ , specific humidity, and temperature with varying degrees over different land cover types possibly due to different prescribed values such as the temperature threshold (Fig. 8, corresponding absolute values in Table S10). Especially, the  $POD_y$  at all sites is most significantly changed when modifying the  $O_3$  concentration by  $\pm 40\%$  (Table S11). Crop is the most sensitive land cover to  $O_3$  changes across the different models ( $8.5\ mmol\ m^{-2}$ ;  $76\%$   $POD_y$  change with respect to the base run), followed by forest ( $10.0\ mmol\ O_3\ m^{-2}$ ;  $59.3\%$ ) and grass ( $14.9\ mmol\ O_3\ m^{-2}$ ;  $56.1\%$ ) which is due to the plant physiognomy (Grulke and Heald et al. ,2020). In a relative sense, the average response change in  $POD_y$  to a  $40\%$  change in  $O_3$  concentrations is the greatest in ZHANG ( $+9.2\ mmol/m^2$ , corresponding to a  $68.1\%$   $POD_y$  change with respect to the base run), followed by CMAQ\_P and TEMIR ( $12$  and  $11.9\ mmol\ O_3\ m^{-2}$  ; $64.8\%$  and  $63.5\%$ ), and then by Web-DO<sub>3</sub>SE ( $11.4\ mmol\ O_3\ m^{-2}$ ;  $53.0\%$ ).





Also, the  $POD_y$  estimate seems to be sensitive to humidity (Q) changes (+/-30%) among all models. At forest, the  $POD_y$  estimates appear to be the most sensitive (4.6 mmol/m<sup>2</sup>; 27.3%), followed by crops (2.9 mmol O<sub>3</sub> m<sup>-2</sup>; 25.9%) and grass (4.6 mmol O<sub>3</sub> m<sup>-2</sup>; 17.3 %). The response is the greatest in TEMIR and CMAQ (between 5.7 and 6.7 mmol m<sup>-2</sup>; 30.7-35.8 %), while it is much smaller for ZHANG (usually close to zero on average). The most non-linear response was shown by Web-DO<sub>3</sub>SE at IT-Cpz which estimated a 5 times higher  $POD_y$  response to increasing humidity than to a humidity decrease pointing towards the strong dryness at this site limiting If temperature is changed by +/-3 K the highest sensitivity was found at crops on average (2.7 mmol O<sub>3</sub> m<sup>-2</sup>; 24.1%), followed by grass (4.6 mmol O<sub>3</sub> m<sup>-2</sup>; 17.2 %) and forest (1.6 mmol m<sup>-2</sup>; 9.5%). The responses unevenly vary in sign depending on the model because the temperature change depends on the optimal temperature at the specific sites. Namely most models estimate a  $POD_y$  decrease when increasing temperature (Fig. 5). As described in Hayes et al. (2019), a temperature increase is seen in southern countries where temperature could limit stomatal uptake since temperature is already close to the optimum in normal conditions. From our sensitivity analysis, temperature impacts on  $POD_y$  are noticeable only for a few sites (e.g., Ambered, Mt. Kenya, and Peru) and models's response to  $POD_y$  change were different due to different thresholds used for the temperature stress factors to stomatal conductance. The greatest changes in magnitude are predicted by Web-DO<sub>3</sub>SE (5.1 mmol O<sub>3</sub> m<sup>-2</sup>; 23.7%), followed by CMAQ\_P (3.1 mmol O<sub>3</sub> m<sup>-2</sup>; 16.7%), ZHANG (1.9 mmol m<sup>-2</sup>; 14.1 %) and TEMIR (1.7 mmol O<sub>3</sub> m<sup>-2</sup>; 9.6 %). In contrast, not all models are sensitive to changes of soil water content (SWC). The greatest response is seen in CMAQ\_P (-6.3 and +1.4 mmol m<sup>-2</sup>; -34.0% and +7.6%), followed by Web-DO<sub>3</sub>SE (-2.2 and -2.2 mmol O<sub>3</sub> m<sup>-2</sup>; -10.2% and -10.2%), and TEMIR (-1.1 and +0.8 mmol O<sub>3</sub> m<sup>-2</sup>; -5.9% and +4.3%), while ZHANG shows no difference in this regard because it is not sensitive to soil moisture. The changes are largest at crops (1.5 mmol O<sub>3</sub> m<sup>-2</sup>; 13.4%), while grass and forest show similar responses (2.8 and 1.7 mmol O<sub>3</sub> m<sup>-2</sup>; 10.5 and 10.1 %, respectively). That is in line with De Marco et al. (2020) who show that  $POD_y$  responses to soil water changes increase with higher Y threshold (here crops). The models do not appear to be sensitive to LAI 14d shifts, with the only exception of Web-DO<sub>3</sub>SE, which simulates a lower  $POD_y$  for both early and late LAI shifts (-2.6 mmol O<sub>3</sub> m<sup>-2</sup> on average, across all land covers). LAI is used as a proxy for growing seasons in most models whereas Web-DO<sub>3</sub>SE considers growing seasons directly.



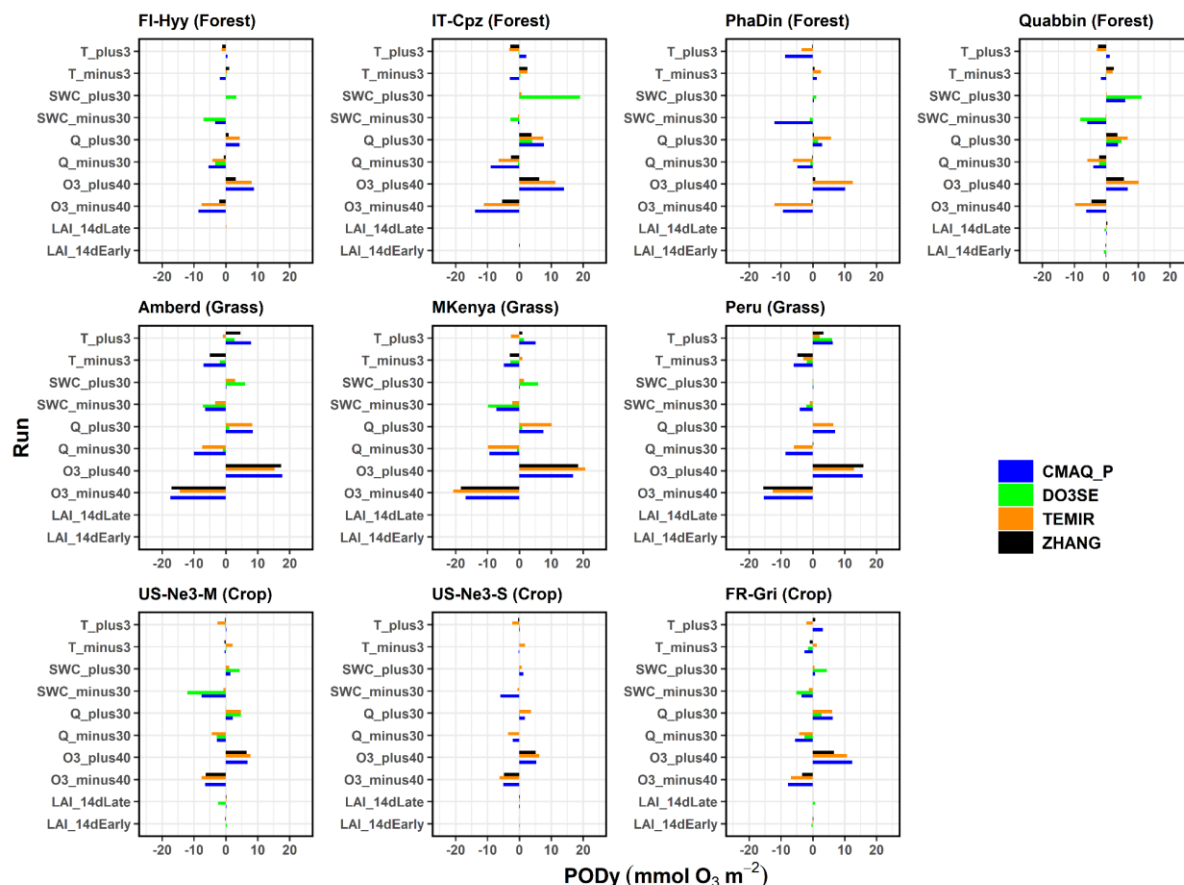


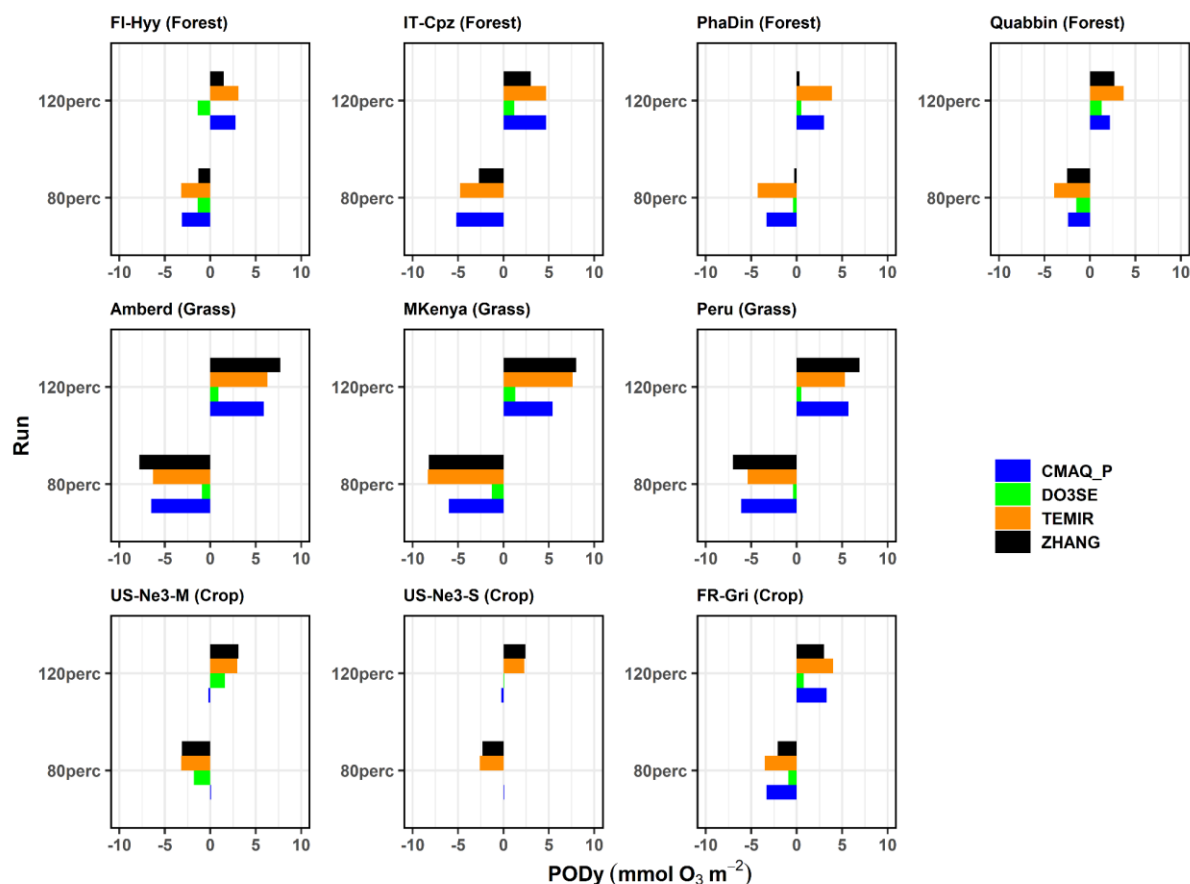
**Fig 8: Meteorology sensitivity assessment: Absolute change of  $POD_y$  values with respect to Base run  $POD_y$  due to 10 or 20 % variation of the temperature (T), soil water content (SWC), absolute humidity (Q),  $O_3$  and LAI/growing season.**

A 20% change of  $g_{max}/V_{c_{max}}$  leads to corresponding changes in  $POD_y$  values. An increase or decrease of the parameter leads to very similar changes (in +/-) (Fig. 9, corresponding data in Table S12 – S14). The response appears to be generally uniform across sites. On average, the results show  $+28.9 \pm 22.4$  %  $POD_y$  change for the 20 % increase of  $g_{max}/V_{c_{max}}$ , and  $-27.4 \pm 13.1$  % for the 20 % decrease with the largest absolute changes at grassland (up to  $8 \text{ mmol m}^{-2}$ , ZHANG). At forests and crops, changes up to 5 and  $3 \text{ mmol m}^{-2}$  occur,



520 respectively. Among all sites, noticeably higher (the highest) relative changes were estimated at FR-Gri which  
 521 thus constituted the only relevant source of variability. This change is significantly different to the change at US-  
 522 Ne3 (20-30 %) which reflects the contrasting low O<sub>3</sub> level at US-Ne3 compared to the highly polluted FR-Gri  
 523 site. Also, the ZHANG model predicts the highest changes at crops while CMAQ\_P seems insensitive. The  
 524 ZHANG (and TEMIR) model appears to be the most sensitive model to the changes at most sites due to the  
 525 strong dependency on the  $g_{\max}/V_{c\max}$  parameter (see analysis above). The only climate trend of the response is  
 526 seen by the ZHANG model which shows an average 65 % increase/decrease in wet forests (PhaDin, FI-Hyy) and  
 527 only a 40 % change in dry places. Sites with very low estimates (PhaDin in ZHANG, Peru in Web-DO<sub>3</sub>SE) were  
 528 excluded from this sensitivity study.

529



530



531 **Fig 9: Land cover parameterisation sensitivity assessment: Absolute change of  $POD_y$  values with respect**  
532 **to the base run  $POD_y$  values due to 20 % variation of  $G_{smax}$  or  $V_{Cmax}$ .**

533

534 To indicate the likely damage, and range of damage that our modelled values of  $POD_y$  predict, we have used  
535  $POD_y$  flux-response relationships available in the literature that most closely represent the vegetation type and  
536 climatic location of each study site (Table 5). To estimate  $O_3$  damage to forests we use recently derived flux-  
537 response relationships that relate  $POD_1$  values to gross annual increment (Karlsson et al., sub) and hence indicate  
538 the annual change in growth rate caused by  $O_3$ . The mean model ensemble estimates a percentage reduction in  
539 gross annual increment of around 5% for FI-Hyy and Pha Din, 6% for IT-Cpz and 14% for Quabbin. However,  
540 the range in estimates across models is not insignificant and most extreme at the Quabbin site with a minimum  
541 of 11% and a maximum of 21% around the mean 13% value; this is due to broadleaf deciduous species being  
542 more sensitive to  $O_3$  dose than needleleaf species and hence more sensitive to a range of  $POD_y$  model  
543 simulations (Bueker et al., 2015). It should also be emphasised that the Pha Din site uses a European-derived  
544 flux-response relationship for an Asian forest site.



						PODy			% Response			
Site	Species	y	Flux-response relationship	Response metric & species	min	median	max	min	median	max	Location of PODy relationship	Reference
FI-Hyy	Scots pine	1	$y = -0.0057x + 1.0015$	Gross Annual Increment (GAI) % for Norway spruce/Scots pine	2.3	10.2	15.1	1.2	5.6	8.5	Europe	Karlsson et al., sub (to TOARII community special issue)
Quabbin	Birch/Beech (Broadleaf deciduous)	1	$y = -0.0093x + 0.9461$	Gross Annual Increment (GAI) % for Birch/Beech	6.5	9.1	16.8	11.4	13.9	21.0	Europe	Karlsson et al., sub (to TOARII community special issue)
PhaDin	Norway spruce (Evergreen needleleaf)	1	$y = -0.0057x + 1.0015$	Gross Annual Increment (GAI) % for Norway spruce/Scots pine	0.4	8.1	20.3	0.0	4.5	11.4	Europe	Karlsson et al., sub (to TOARII community special issue)
IT-Cpz	Holm oak	1	$y = -0.0047x + 1.001$	Gross Annual Increment (GAI) % for Aleppo pine/Holm Oak	2.8	13.3	25.8	1.2	6.2	12.0	Europe	Karlsson et al., sub (to TOARII community special issue)
FR-Gri	winter wheat	6	$y = -0.0385x + 1.003$	% grain yield loss for wheat	3.6	6.8	9.3	13.6	25.9	35.5	Europe	UNECE LRTAP Mapping Manual (2017)
US-Ne3 (Maize)	Maize	6	$y = 0.0426x + 1$	% grain yield loss for wheat	10.5	12.4	13.6					Peng, J., Shang, B., Xu, Y., Feng, Z., Pleijel, H. and Calatayud, V., 2019. Ozone exposure-and flux-yield response relationships for maize. Environmental pollution, 252, pp.1-7.
US-Ne3 (Soybean)	Soybean	6	$y = -0.033x + 1.01$	% relative seed yield loss per soybean plant	0.0	8.3	11.0	0.0	26.4	35.3	China	Zhang, W., Feng, Z., Wang, X., Liu, X., Hu, E. (2017) Quantification of ozone exposure-and stomatal uptake-yield response relationships for soybean in Northeast China. Sci of the Total



												Env., 599-600 (710-720)	
Amber d	Grasslan d	1	y = -0.0062x + 0.947	% total biomass loss for temperate perennial grassland	7.9	29.4	34.1	10.2	23.5	26.4	Europe	UNECE Mapping (2017)	LRTAP Manual
MKenya	Grasslan d	1	y = -0.0062x + 0.947	% total biomass loss for temperate perennial grassland	10.9	31.0	37.4	12.1	24.5	28.5	Europe	UNECE Mapping (2017)	LRTAP Manual
Peru	Grasslan d	1	y = -0.0062x + 0.947	% total biomass loss for temperate perennial grassland	2.6	22.1	26.6	6.9	19.0	21.8	Europe	UNECE Mapping (2017)	LRTAP Manual

**Table 5. Estimates of O<sub>3</sub> damage (for specific response metrics) derived from using the ensemble mean modelled PODy values (and minimum and maximum values) with appropriate flux-response relationships based on land cover type. The climatic location within which the flux-response relationships are derived are stated to show the relevance of their use in estimating damage. Shaded cells denote flux-response relationships that are derived outside of the broad climate region to which they are applied in this study and hence whose damage estimates should be treated with caution.**

For crops, flux response relationships are available for wheat, maize and soybeans (UNECE LRTAP, 2017, Peng et al., 2019 and Zhang et al., 2017). These relationships are derived from Europe (wheat) and China (maize and soybean). For wheat, we see a large range in percentage yield loss with a mean model ensemble of 26 % but a maximum yield loss of 35 %. This is driven by high POD<sub>6</sub> values derived from CMAQ\_P and TEMIR. For maize at US-Ne3 the results are very consistent with relative grain yield loss estimates ranging from 1.4 to 1.6 %. For soybeans at US-Ne3, the results are less consistent than maize with a minimum and maximum of 0 and 35 % yield around a mean of 26 %. It is important to note that a Chinese-derived flux-response relationship is used to estimate O<sub>3</sub> damage on both US-grown crops.



561 Finally, for grasslands, we estimate total biomass losses of 19, 24 and 23% from the ensemble model mean for Peru, Mt  
 562 Kenya and Amberd respectively. The range in model values is relatively small for Amberd and Mt Kenya. A low minimum  
 563 value of 6 % total biomass loss is estimated for Peru due to the Web-DO<sub>3</sub>SE model having a very low POD<sub>y</sub> at this location  
 564 due to a likely oversensitive limitation to O<sub>3</sub> uptake caused by low temperatures.

565

#### 566 4. Discussion and Conclusion

567 Here we have compared six deposition schemes commonly used in atmospheric chemistry transport models. We have  
 568 focussed on the stomatal component of deposition since this is acknowledged to have a substantial influence on damage to  
 569 vegetation, and ultimately the ability of these six models to estimate the POD<sub>y</sub> metric designed to indicate the level of O<sub>3</sub>  
 570 damage to forest, crops and grasslands. The models estimate POD<sub>y</sub> values of 28, 15 and 9 mmol O<sub>3</sub> m<sup>-2</sup> for grassland, forests  
 571 and crops, respectively. The multi-model mean estimates are generally in the expected range which suggests that the  
 572 stomatal flux output of these models could be used for O<sub>3</sub> impact assessments. We also explored the differences in POD<sub>y</sub> by  
 573 geographical location. When comparing one vegetation type, we find multiple drivers including O<sub>3</sub> concentration. The  
 574 different model types are not the driving force, instead, the models can predict similar results.

575 There are three key reasons for differences in dry deposition model estimates i. model construct and the inclusion/exclusion  
 576 of important factors that determine G<sub>st</sub> and G<sub>sun</sub>; ii. model parameterisation which may characterise the land cover types and  
 577 iii. differing model sensitivity to climate variables (seasonal, location effects) in estimates of stomatal deposition. The model  
 578 comparison of stomatal conductance and stomatal dry deposition for ozone helps us to understand the differences between  
 579 models. We found that models simulate generally reasonable stomatal deposition of 0.5 -0.8 cm s<sup>-1</sup> in summer whereas the  
 580 different model types often agree very well with each other. The stomatal conductance estimates among the models agree  
 581 with correlation coefficients of 0.75, 0.80 and 0.85 for forests, crops and grasslands. The model differences, identified during  
 582 this analysis, can be explained by the model's dependence on the meteorological conditions at sites. Indeed, both model  
 583 structure (e.g. Raghav, Kumar and Liu 2023) and parameters (Fares et al., 2013) can affect the accuracy of stomatal  
 584 conductance models. However, studies have shown that when properly calibrated against field observations, structurally  
 585 different stomatal models can produce similar stomatal conductance (Fares et al., 2013, Mäkela et al., 2019). Calibrating the  
 586 key parameters of stomatal conductance models (e.g. g<sub>max</sub>/Vc<sub>max</sub>) is a crucial next step to improve the accuracy of stomatal  
 587 conductance and POD<sub>y</sub> estimates, as our sensitivity tests show direct, and possible non-linear relationship between POD<sub>y</sub> and  
 588 g<sub>max</sub>/Vc<sub>max</sub> (e.g. at FR-Gri). This is possible with the recent availability of standardised global eddy flux (FLUXNET,  
 589 Pastorello et al., 2020) and sap flow (SAPFLUXNET, Poyatos et al., 2020) data.



590 To estimate  $POD_y$  for a representative leaf of the upper canopy, the sunlit leaf must be distinguished from the total leaf.  
 591 Since the effects-based community recognised that sunlit leaves contribute most to carbon assimilation throughout the  
 592 growing season or  $O_3$ -sensitive period (e.g. in wheat, this is considered to be the time from anthesis to maturity) and hence it  
 593 will better represent damaging  $O_3$  uptake. All flux response relationships for  $POD_y$  are developed for such a representative  
 594 leaf. This is an important distinction since previous model comparison studies (e.g. Clifton et al., 2023) have tended to focus  
 595 on whole canopy dynamics. These are important to estimate accurately, but to estimate  $POD_y$  requires additional canopy  
 596 level processes, which need i.  $O_3$  concentration at the top of the canopy, ii. wind speed at the top of the canopy and iii.  $G_{sun}$   
 597 of a representative leaf at the top of the canopy.

598 Our models estimate 30-50 % of stomatal  $O_3$  deposition at sunlit leaves. Thereby, the model estimates of the total stomatal  
 599 flux are more widespread (during one season) than the estimates of the sunlit only which suggests an important role of the  
 600 model's partitioning in two big leaves. When calculating  $POD_y$  model means estimates generally agree with the literature but  
 601 most discrepancies between model estimates of  $POD_y$  ultimately come down to the differences in simulations of stomatal  
 602 conductance. The sensitivity analysis of  $POD_y$  yields ozone as the most important input variable, to whose changes all  
 603 models respond similarly. Considering all models and sites together,  $POD_y$  were affected most by the  $O_3$  concentration (+-  
 604 60-80 % site-dependent, i.e., higher  $O_3$  conc leads to higher  $POD_y$ ), followed by humidity (30-50 % site-dependent impact).  
 605 Soil moisture impacts were also significant for the CMAQ\_P and Web-DO<sub>3</sub>SE model (up to +-68 % and 22 % change). The  
 606 sensitivity to temperature changes varies strongly among the model and its parametrization. As the plant canopy acts as a  
 607 persistent sink of  $O_3$ , there is a significant vertical gradient of  $O_3$  within the atmospheric surface layer. For example, Travis  
 608 et al. (2019) show that the midday  $O_3$  concentration at 65 m above ground (mid-point of a first vertical layer of GEOS-Chem  
 609 v9-02) is 3 ppb higher than the  $O_3$  concentration at 10 m above ground (inferred by Monin-Obukhov Similarity Theory,  
 610 MOST) over the Southeastern United States. A mismatch between  $O_3$  measurement height and canopy height can lead to  
 611 inaccurate  $POD_y$  calculation (Gerosa et al, 2017). As we show that the errors in  $O_3$  concentrations propagate non-linearly to  
 612  $POD_y$  (i.e. 40% changes in  $O_3$  leads to 53 - 68 % changes in  $POD_y$ ), such a mismatch should be carefully avoided by  
 613 applying atmospheric surface layer theories (e.g. MOST) to estimate the vertical profile of  $O_3$ , and therefore the canopy-top  
 614  $O_3$  concentration, if direct measurement or model output of  $O_3$  at canopy top is not available.

615

616 Finally, we use flux-response relationships for temperate deciduous (Beech/birch), temperate needleleaf (Norway spruce  
 617 (*Picea abies*)), crops (wheat (*Triticum aestivum*), maize (*Zea mays*) and soybeans (*Glycine max*)) and grassland (*Lolium*  
 618 *perenne*) to give a suggest the potential likely variation of damage estimates by land cover type and climatic region. These  
 619 relationships have predominantly been developed for European and Asia forest and crop species. Therefore, they should be  
 620 applied to other climate regions with caution although recent evidence suggests that tropical forest species may have similar



621 sensitivity to  $O_3$  as European species (Cheeseman et al. 2024). Although there is rather large variability in  $POD_y$  values  
 622 estimated by the model, the median values are relatively robust. Unfortunately, there is only statistical or modelled evidence  
 623 of actual  $O_3$  damage, and only at a few of the sites investigated. Modelled evidence uses stomatal ozone flux models similar  
 624 to those used in this study, but which have been parameterised for local site conditions (Stella et al., 2013 for FR-Gri wheat).  
 625 Simulations with a terrestrial biosphere model suggested an average long-term  $O_3$  inhibition of 10.4% for the period 1992–  
 626 2011 at the Harvard site (Yue et al 2016); this compares to our model ensemble estimate of 14% GAI biomass loss for  
 627 Quabbin. A significant but small NEP reduction was found during Spring in the Italian Castelporziano forest site (up to -  
 628 1.37 %) but not at the FI-Hyy or FR-Gri sites (Savi et al., 2020). Our modelling estimated substantially lower  $POD_y$  values  
 629 and associated damage at Hyy and IT-Cpz than Quabbin though we would expect to see a more substantial  $O_3$  effect than  
 630 that demonstrated by the NEP statistical modelling (i.e. 5 and 6% GAI biomass loss at FI-Hyy and IT-Cpz respectively).  
 631 Similar simulations with a different terrestrial biosphere model found only moderate  $O_3$  damage effects (GPP reductions of  
 632 4–6 %; Yue & Unger, 2014). This result is driven by low ambient ozone concentrations but also by the choice of a C4  
 633 photosynthetic mechanism to estimate stomatal conductance which gives relatively high-water use efficiency). These  
 634 simulations also suggested that the US-Ne3 experienced a higher ozone effect on GPP than Harvard which is consistent with  
 635 our modeling for soybeans (but not maize, generally considered an  $O_3$  tolerant crop species; Mills et al 2011). According to  
 636 the  $POD_6$  estimates made using a SURFATM model, parameterised for Grignon wheat,  $POD_6$  values of  $1.094 \text{ mmol } O_3 \text{ m}^{-2}$   
 637 were estimated from 1 April to 1 July 2009 which compared with our range of 3.6 to 9.3; the locally parameterised values  
 638 gave estimated crop yield losses of 4.2%, compared to our median model ensemble estimates of 25% for the winter wheat.  
 639 This is most likely due to the lower  $g_{max}$  value used in the local parameterisation ( $296 \text{ mmol } O_3 \text{ m}^{-2} \text{ s}^{-1}$ ). However, no  
 640 recording of actual damage is given at the FR-Gri site, so it is not possible to tell which of these simulated damage estimates  
 641 is closer to reality.

642 The experiments performed here with varying climate and vegetation input data also find a similar sensitivity of  $POD_y$  to  $O_3$ .  
 643 It is helpful to have a range of models and model constructs in deposition schemes especially where these have been  
 644 developed for particular land cover types. When used in damage estimates it is important to ensure that key stressors are  
 645 included which may be important for that respective geographical region (such as soil and vapour pressure deficit).  
 646 Recognising that several deposition schemes would be able to reliably predict  $POD_y$  for different climates and cover types  
 647 once they have been parameterised appropriately will extend the usefulness of flux-response relationships.

648 All in all, we have demonstrated, through this paper, the widespread applicability and consensus among various numerical  
 649 stomatal flux methods and identified the key model constructs and parameterisations that cause differences in ozone  
 650 deposition and  $POD_y$  estimates. Our results and findings present exciting opportunities, enabling us to extend the application  
 651 beyond specific sites and growing seasons, to conduct comprehensive global stomatal flux studies over long periods.





Integrating the TOAR database with the Web-DO<sub>3</sub>SE model enables automatic models runs for ozone-vegetation impact assessment at a large range of sites using the TOAR database.

654

655

#### 656 **Author contributions**

657 T.E.: site selection, TOAR data extraction, data preparation, model support, modelling Web-DO<sub>3</sub>SE, writing, coordination.  
658 A.M.: modelling (ZHANG, MESSy, NOAH-GEM, TEMIR model), statistics, plots and analysis. L.E.: concept, writing.  
659 H.M.: writing, reviewing. L.Z.: concept and writing. L.R.: modelling with CMAQ, FLUXNET data preparation. C.B.:  
660 debugging and test simulations of Web-DO<sub>3</sub>SE. A.W.: site selection, preparation of FLUXNET and sensitivity data. G.K.:  
661 site selection, TOAR data extraction. G.G.: site analysis. M.H.: plots and reviewing. P.G.: PODy analysis.

662

#### 663 **Competing interests**

664 The authors have no competing interests.

665

#### 666 **Acknowledgements**

667 We acknowledge the TOAR team supports the data extraction. The authors acknowledge the access to the meteorological  
668 data on the Jülich MeteoCloud provided by Jülich Supercomputing Centre (Krause et al., 2018). We thank the responsible  
669 people of the selected measurement sites for their support in obtaining site information. We greatly appreciate helpful  
670 discussions in the earlier stages of the project from the following people: Owen Cooper, Zhaozhong Feng, Laurens  
671 Ganzeveld, Meiyun Lin, Martin Schultz, Eran Tas, and Oliver Wild.

672

#### 673 **Code availability**

674 The Web-DO<sub>3</sub>SE source code is freely available at <https://toar-data.fz-juelich.de/> under the CC-BY 4.0 license  
675 (<https://creativecommons.org/licenses/by/4.0/>). The further model code can be obtained upon request.

676

#### 677 **Data availability**

678 The TOAR data is freely available at <https://toar-data.fz-juelich.de/> under the CC-BY 4.0 license  
679 (<https://creativecommons.org/licenses/by/4.0/>). The ERA5 data used can be downloaded from the MeteoCloud server  
680 (<https://datapub.fz-juelich.de/slcs/meteocloud/index.html>). FLUXNET 2015 dataset is publicly available at  
681 <https://fluxnet.org/data/fluxnet2015-dataset/>. Stomatal conductance estimates, and the related FLUXNET 2015 data from  
682 SynFlux version 2 can be obtained by contacting Christopher Holmes ([cdholmes@fsu.edu](mailto:cdholmes@fsu.edu)).

683



## 684 References

- 685 Ainsworth, E. A., Yendrek, C. R., Sitch, S., Collins, W. J., and Emberson, L. D.: The effects of tropospheric ozone on net  
 686 primary productivity and implications for climate change. *Annual review of plant biology*, 63(1), 637–661,  
 687 <https://doi.org/10.1146/annurev-arplant-042110-103829>, 2012.
- 688
- 689 Ainsworth, E. A.: Understanding and improving global crop response to ozone pollution. *The Plant Journal*, 90(5), 886–897,  
 690 <https://doi.org/10.1111/tpj.13298>, 2017.
- 691
- 692 Avnery, S., Mauzerall, D. L., Liu, J., and Horowitz, L. W.: Global Crop Yield Reductions due to Surface Ozone Exposure: 1.  
 693 Year 2000 Crop Production Losses and Economic Damage, *Atmos. Environ.*, 45, 2284–2296,  
 694 <https://doi.org/10.1016/j.atmosenv.2010.11.045>, 2011.
- 695
- 696 Aguilos, M., Hérault, B., Burban, B., Wagner, F., & Bonal, D.: What drives long-term variations in carbon flux and balance  
 697 in a tropical rainforest in French Guiana?. *Agricultural and forest meteorology*, 253, 114–123,  
 698 <https://doi.org/10.1016/j.agrformet.2018.02.009>, 2018.
- 699
- 700 Amos, B., Arkebauer, T. J., and Doran, J. W.: Soil surface fluxes of greenhouse gases in an irrigated maize-based  
 701 agroecosystem. *Soil Science Society of America Journal*, 69(2), 387–395, <https://doi.org/10.2136/sssaj2005.0387>, 2015.
- 702
- 703 Beck, H. E., McVicar, T.R., Vergopolan, N. Berg, A., Lutsko, N. J., Dufour, A., Zeng, Z., Jiang, X., van Dijk, A. I. J. M.,  
 704 and Miralles, D. G.: High-resolution (1 km) Köppen-Geiger maps for 1901–2099 based on constrained CMIP6 projections.  
 705 *Sci Data* 10, 724, <https://doi.org/10.1038/s41597-023-02549-6>, 2023.
- 706
- 707 Broberg, M. C., Feng, Z., Xin, Y., and Pleijel, H.: Ozone effects on wheat grain quality—A summary. *Environmental*  
 708 *Pollution*, 197, 203–213, <https://doi.org/10.1016/j.envpol.2014.12.009>, 2015
- 709
- 710 Büker, P., Feng, Z., Uddling, J., Briolat, A., Alonso, R., Braun, S., Elvira, S., Gerosa, G., Karlsson, P.E., Le Thiec, D. and  
 711 Marzuoli, R., 2015.: New flux based dose–response relationships for ozone for European forest tree species. *Environmental*  
 712 *Pollution*, 206, pp.163–174. <https://doi.org/10.1016/j.envpol.2015.06.033>, 2015.
- 713
- 714 Bukowiecki, N., Steinbacher, M., Henne, S., Nguyen, N.A., Nguyen, X.A., Hoang, A.L., Nguyen, D.L., Duong, H.L.,  
 715 Engling, G., Wehrle, G., Gysel-Beer, M. and Baltensperger, U.: Effect of Large-scale Biomass Burning on Aerosol Optical



- 716 Properties at the GAW Regional Station Pha Din, Vietnam. *Aerosol Air Qual. Res.* 19: 1172-1187, <https://doi.org/10.4209/aaqr.2018.11.0406>, 2019.
- 717
- 718
- 719 Clifton, O. E., Fiore, A. M., Munger, J. W., and Wehr, R.: Spatiotemporal controls on observed daytime ozone deposition
- 720 velocity over northeastern US forests during summer. *Journal of Geophysical Research: Atmospheres*, 124(10), 5612-5628,
- 721 <https://doi.org/10.1029/2018JD029073>, 2019.
- 722
- 723 Clifton, O. E., D. L. Lombardozzi, A. M. Fiore, F. Paulot, and L. W. Horowitz.: Stomatal conductance influences interannual
- 724 variability and long-term changes in regional cumulative plant uptake of ozone. *Environmental Research Letters*.
- 725 <https://doi.org/10.1088/1748-9326/abc3f1>, 2020a.
- 726
- 727 Clifton, O. E., Paulot, F., Fiore, A. M., Horowitz, L. W., Correa, G., Baublitz, C. B., ... and Weng, E.: Influence of dynamic
- 728 ozone dry deposition on ozone pollution. *Journal of Geophysical Research: Atmospheres*, 125(8), <https://doi.org/10.1029/2020JD032398>, 2020b.
- 729
- 730
- 731 Clifton, O. E., Schwede, D., Hogrefe, C., Bash, J. O., Bland, S., Cheung, P., Coyle, M., Emberson, L., Flemming, J., Fredj,
- 732 E., Galmarini, S., Ganzeveld, L., Gazetas, O., Goded, I., Holmes, C. D., Horváth, L., Huijnen, V., Li, Q., Makar, P. A.,
- 733 Mammarella, I., Manca, G., Munger, J. W., Pérez-Camanyo, J. L., Pleim, J., Ran, L., San Jose, R., Silva, S. J., Staebler, R.,
- 734 Sun, S., Tai, A. P. K., Tas, E., Vesala, T., Weidinger, T., Wu, Z., and Zhang, L.: A single-point modeling approach for the
- 735 intercomparison and evaluation of ozone dry deposition across chemical transport models (Activity 2 of AQMEII4), *Atmos.*
- 736 *Chem. Phys.*, 23, 9911–9961, <https://doi.org/10.5194/acp-23-9911-2023>, 2023.
- 737
- 738 Chen, X., Quéléver, L. L. J., Fung, P. L., Kesti, J., Rissanen, M. P., Bäck, J., Keronen, P., Junninen, H., Petäjä, T.,
- 739 Kerminen, V.-M., and Kulmala, M.: Observations of ozone depletion events in a Finnish boreal forest, *Atmos. Chem. Phys.*,
- 740 18, 49–63, <https://doi.org/10.5194/acp-18-49-2018>, 2018 .
- 741
- 742 Copernicus Climate Change Service (C3S) (2017): ERA5: Fifth generation of ECMWF atmospheric reanalyses of the global
- 743 climate. Copernicus Climate Change Service Climate Data Store (CDS), date of access: 27.11.2024.
- 744 <https://cds.climate.copernicus.eu/cdsapp#!/home>
- 745
- 746 De Marco, A., Anav, A., Sicard, P., Feng, Z., and Paoletti, E.: High spatial resolution ozone risk-assessment for Asian
- 747 forests. *Environmental Research Letters*, 15(10), 104095, <https://doi.org/10.1088/1748-9326/abb501>, 2020.
- 748



- 749 Ducker, J. A., Holmes, C. D., Keenan, T. F., Fares, S., Goldstein, A. H., Mammarella, I., Munger, J. W. and Schnell, J.:  
 750 Synthetic ozone deposition and stomatal uptake at flux tower sites. *Biogeosciences*, 15(17), 5395-5413, [https://doi.org](https://doi.org/10.5194/bg-15-5395-2018)  
 751 [/10.5194/bg-15-5395-2018](https://doi.org/10.5194/bg-15-5395-2018), 2018.
- 752
- 753 Emberson, L.: Effects of ozone on agriculture, forests and grasslands. *Philosophical Transactions of the Royal Society A*,  
 754 378(2183), 20190327, <https://doi.org/10.1098/rsta.2019.0327>, 2020.
- 755
- 756 Emmerichs, T.; Kerkweg, A.; Ouwersloot, H.; Fares, S.; Mammarella, I.; Taraborrelli, D.: A Revised Dry Deposition  
 757 Scheme for Land–Atmosphere Exchange of Trace Gases in ECHAM/MESSy v2.54. *Geoscientific Model Development*, 14  
 758 (1), 495–519. <https://doi.org/10.5194/gmd-14-495-2021>, 2021.
- 759
- 760 Fares, S., Mereu, S., Scarascia Mugnozza, G., Vitale, M., Manes, F., Frattoni, M., ... and Loreto, F.: The ACCENT-  
 761 VOCBAS field campaign on biosphere-atmosphere interactions in a Mediterranean ecosystem of Castelporziano (Rome):  
 762 site characteristics, climatic and meteorological conditions, and eco-physiology of vegetation. *Biogeosciences*, 6(6), 1043-  
 763 1058, <https://doi.org/10.5194/bg-6-1043-2009>, 2009.
- 764
- 765 Fares, S. Measured and modelled stomatal and non-stomatal ozone fluxes in a mixed Mediterranean forest. In 25th ICP-  
 766 Vegetation Task Force Meeting. gennaio–2 febbraio 2012, Brescia, Italia.,2012.
- 767
- 768 Fares, S., Savi, F., Muller, J., Matteucci, G., and Paoletti, E.: Simultaneous measurements of above and below canopy ozone  
 769 fluxes help partitioning ozone deposition between its various sinks in a Mediterranean Oak Forest. *Agricultural and Forest*  
 770 *Meteorology*, 198, 181-191. <https://doi.org/10.1016/j.agrformet.2014.08.014>, 2014.
- 771
- 772 Fares, S., Matteucci, G., Mugnozza, G. S., Morani, A., Calfapietra, C., Salvatori, E., ... and Loreto, F. : Testing of models of  
 773 stomatal ozone fluxes with field measurements in a mixed Mediterranean forest. *Atmospheric environment*, 67, 242-251,  
 774 <https://doi.org/10.1016/j.atmosenv.2012.11.007>, 2013.
- 775
- 776 Feng, Z., Tang, H., Uddling, J., Pleijel, H., Kobayashi, K., Zhu, J., ... and Guo, W.: A stomatal ozone flux–response  
 777 relationship to assess ozone-induced yield loss of winter wheat in subtropical China. *Environmental pollution*, 164, 16-23.  
 778 <https://doi.org/10.1016/j.envpol.2012.01.014>, 2012.
- 779



- 780 Fowler, D., Flechard, C., Cape, J.N. et al.: Measurements of Ozone Deposition to Vegetation Quantifying the Flux, the  
 781 Stomatal and Non-Stomatal Components. *Water, Air, & Soil Pollution* 130, 63–74. [https://doi.org](https://doi.org/10.1023/A:1012243317471)  
 782 [/10.1023/A:1012243317471](https://doi.org/10.1023/A:1012243317471), 2001.
- 783
- 784 Fuhrer, J., Val Martin, M., Mills, G., Heald, C. L., Harmens, H., Hayes, F., ... and Ashmore, M. R.: Current and future ozone  
 785 risks to global terrestrial biodiversity and ecosystem processes. *Ecology and evolution*, 6(24), 8785-8799. [https://doi.org](https://doi.org/10.1002/ece3.2568)  
 786 [/10.1002/ece3.2568](https://doi.org/10.1002/ece3.2568), 2016.
- 787
- 788 Ganzeveld, L., & Lelieveld, J.: Dry deposition parameterization in a chemistry general circulation model and its influence on  
 789 the distribution of reactive trace gases. *Journal of Geophysical Research: Atmospheres*, 100(D10), 20999-21012.  
 790 [https://doi.org /10.1029/95JD02266](https://doi.org/10.1029/95JD02266), 1995.
- 791
- 792 Gerosa, G., Vitale, M., Finco, A., Manes, F., Denti, A. B. and Cieslik, S.: Ozone uptake by an evergreen Mediterranean  
 793 Forest (*Quercus ilex*) in Italy. Part I: Micrometeorological flux measurements and flux partitioning. *Atmospheric*  
 794 *Environment*, 39(18), 3255-3266, [https://doi.org /10.1016/j.atmosenv.2005.01.056](https://doi.org/10.1016/j.atmosenv.2005.01.056), 2005.
- 795
- 796 Gerosa, G., Marzuoli, R., Monteleone, B., Chiesa, M., and Finco, A.: Vertical ozone gradients above forests. Comparison of  
 797 different calculation options with direct ozone measurements above a mature forest and consequences for ozone risk  
 798 assessment. *Forests*, 8(9), 337. [https://doi.org /10.3390/f8090337](https://doi.org/10.3390/f8090337), 2017.
- 799 Gerosa G., Marzuoli R., Finco A.: Interannual variability of ozone fluxes in a broadleaf deciduous forest in Italy.  
 800 *ELEMENTA: Science of the Anthropocene* 10(1), 00105. [https://doi.org /10.1525/elementa.2021.00105](https://doi.org/10.1525/elementa.2021.00105), 2022.
- 801 Guaita P.R., Marzuoli R., Gerosa G.A.: A regional scale flux-based O<sub>3</sub> risk assessment for winter wheat in northern Italy,  
 802 and effects of different spatio-temporal resolutions. *Environmental Pollution* 333, 121860, [https://doi.org](https://doi.org/10.1016/j.envpol.2023.121860)  
 803 [10.1016/j.envpol.2023.121860](https://doi.org/10.1016/j.envpol.2023.121860), 2023.
- 804 Hardacre, C., Wild, O., and Emberson, L.: An evaluation of ozone dry deposition in global scale chemistry climate models,  
 805 *Atmos. Chem. Phys.*, 15, 6419–6436, [https://doi.org /10.5194/acp-15-6419-2015](https://doi.org/10.5194/acp-15-6419-2015), 2015.
- 806 Hayes, F., Mills, G., Alonso, R., González-Fernández, I., Coyle, M., Grünhage, L., ... and Marzuoli, R.: A site-specific  
 807 analysis of the implications of a changing ozone profile and climate for stomatal ozone fluxes in Europe. *Water, Air, & Soil*  
 808 *Pollution*, 230, 1-15, [https://doi.org /10.1007/s11270-018-4057-x](https://doi.org/10.1007/s11270-018-4057-x), 2019.



- 809 Henne, S., Junkermann, W., Kariuki, J. M., Aseyo, J. and Klausen, J.: Mount Kenya Global Atmosphere Watch Station  
 810 (MKN): Installation and Meteorological Characterization. *J. Appl. Meteor. Climatol.*, 47, 2946–2962, [https://doi.org/](https://doi.org/10.1175/2008JAMC1834.1)  
 811 [/10.1175/2008JAMC1834.1](https://doi.org/10.1175/2008JAMC1834.1), 2008a.
- 812 Henne, S., Klausen, J., Junkermann, W., Kariuki, J. M., Aseyo, J. O., and Buchmann, B.: Representativeness and  
 813 climatology of carbon monoxide and ozone at the global GAW station Mt. Kenya in equatorial Africa, *Atmos. Chem. Phys.*,  
 814 8, 3119–3139, <https://doi.org/10.5194/acp-8-3119-2008>, 2008b.
- 815 Hersbach, H., Bell, B., Berrisford, P., Hirahara, S., Horányi, A., Muñoz-Sabater, J., ... and Thépaut, J. N.: The ERA5 global  
 816 reanalysis. *Quarterly Journal of the Royal Meteorological Society*, 146(730), 1999–2049, <https://doi.org/10.1002/qj.3803>,  
 817 2020.
- 818 Horváth, L., Koncz, P., Möring, A. et al.: An Attempt to Partition Stomatal and Non-stomatal Ozone Deposition Parts on a  
 819 Short Grassland. *Boundary-Layer Meteorol* 167, 303–326, <https://doi.org/10.1007/s10546-017-0310-x>, 2018.
- 820 Huang, M., Crawford, J. H., Carmichael, G. R., Bowman, K. W., Kumar, S. V., and Sweeney, C.: Satellite soil moisture data  
 821 assimilation impacts on modeling weather variables and ozone in the southeastern US – Part 2: Sensitivity to dry-deposition  
 822 parameterizations, *Atmos. Chem. Phys.*, 22, 7461–7487, <https://doi.org/10.5194/acp-22-7461-2022>, 2022.  
 823
- 824 Jägermeyr, J., Müller, C., Minoli, S., Ray, D., and Siebert, S.: GGCM Phase 3 crop calendar [Data set]. Zenodo.  
 825 <https://doi.org/10.5281/zenodo.5062513>, 2021a.  
 826
- 827 Jägermeyr et al.: Climate impacts on global agriculture emerge earlier in new generation of climate and crop, *Nature Food*,  
 828 2, 873–885, <https://www.nature.com/articles/s43016-021-00400-y>, 2021b.  
 829
- 830 Junninen, H., Lauri, A., Keronen, P., Aalto, P., Hiltunen, V., Hari, P., Kulmala, M. 2009. Smart-SMEAR: online data  
 831 exploration and visualization tool for SMEAR stations. *Boreal Environment Research* 14, 447–457,  
 832 <http://www.borenv.net/BER/pdfs/ber14/ber14-447.pdf>, 2009.  
 833
- 834 Grulke, N. E. and Heath, R. L.: Ozone effects on plants in natural ecosystems. *Plant Biology*, 22, 12–37.  
 835 <https://doi.org/10.1111/plb.12971>, 2020.  
 836



- 837 Khan, A. M., Clifton, O. E., Bash, J. O., Bland, S., Booth, N., Cheung, P., ... and Stoy, P. C.: Ozone dry deposition through  
 838 plant stomata: Multi-model comparison with flux observations and the role of water stress as part of AQMEII4 Activity 2.  
 839 EGU sphere, 2024, 1-34. <https://doi.org/10.5194/egusphere-2024-3038>, 2024.
- 840
- 841 Kattge, J. and Knorr, W.: Temperature acclimation in a biochemical model of photosynthesis: a reanalysis of data from 36  
 842 species. *Plant, cell & environment*, 30(9), 1176-1190, <https://doi.org/10.1111/j.1365-3040.2007.01690.x>, 2007.
- 843
- 844 Krause, D., & Thörnig, P.: JURECA: modular supercomputer at Jülich supercomputing centre. *Journal of large-scale*  
 845 *research facilities JLSRF*, 4, A132-A132, <https://doi.org/10.17815/jlsrf-4-121-1>, 2018.
- 846
- 847 Li, M., Wu, P., & Ma, Z.: A comprehensive evaluation of soil moisture and soil temperature from third-generation  
 848 atmospheric and land reanalysis data sets. *Int. J. Climatol*, 40(13), 5744-5766, <https://doi.org/10.1002/joc.6549>, 2020.
- 849
- 850 Leung, F., Williams, K., Sitch, S., Tai, A. P., Wiltshire, A., Gornall, J., ... and Scoby, D.: Calibrating soybean parameters in  
 851 JULES 5.0 from the US-Ne2/3 FLUXNET sites and the SoyFACE-O<sub>3</sub> experiment. *Geoscientific Model*  
 852 *Development*, 13(12), 6201-6213, doi: 10.5194/gmd-13-6201-2020, 2020.
- 853
- 854 Mäkelä, J., Knauer, J., Aurela, M., Black, A., Heimann, M., Kobayashi, H., ... and Aalto, T.: Parameter calibration and  
 855 stomatal conductance formulation comparison for boreal forests with adaptive population importance sampler in the land  
 856 surface model JSBACH. *Geoscientific Model Development*, 12(9), 4075-4098. <https://doi.org/10.5194/gmd-12-4075-2019>,  
 857 2019.
- 858
- 859 McGrath, J. M., Betzelberger, A. M., Wang, S., Shook, E., Zhu, X. G., Long, S. P., & Ainsworth, E. A.: An analysis of  
 860 ozone damage to historical maize and soybean yields in the United States. *Proceedings of the National Academy of Sciences*,  
 861 112(46), 14390-14395, <https://doi.org/10.1073/pnas.1509777112>, 2015.
- 862
- 863 Meszaros, R., Horváth, L., Weidinger, T., Neftel, A., Nemitz, E., Dämmgen, U., ... and Loubet, B.: Measurement and  
 864 modelling ozone fluxes over a cut and fertilized grassland. *Biogeosciences*, 6(10), 1987-1999.  
 865 <https://doi.org/10.5194/bg-6-1987-2009>, 2009.
- 866
- 867 Meyers, T. P., Finkelstein, P., Clarke, J., Ellestad, T. G., and Sims, P. F.: A multilayer model for inferring dry deposition  
 868 using standard meteorological measurements. *Journal of Geophysical Research: Atmospheres*, 103(D17), 22645-22661,  
 869 <https://doi.org/10.1029/98JD01564>, 1998.



- 870
- 871 Mills, G., Hayes, F., Simpson, D., Emberson, L., Norris, D., Harmens, H. and Büker, P., Evidence of widespread effects of  
 872 ozone on crops and (semi-)natural vegetation in Europe (1990–2006) in relation to AOT40- and flux-based risk maps. *Global*  
 873 *Change Biology*, 17: 592–613, <https://doi.org/10.1111/j.1365-2486.2010.02217.x>, 2011.
- 874
- 875 Mills, G., Pleijel, H., Malley, C. S., Sinha, B., Cooper, O. R., Schultz, M. G., Neufeld, H. S., Simpson, D., Sharps, K., Feng,  
 876 Z., Gerosa, G., Harmens, H., Kobayashi, K., Saxena, P., Paoletti, E., Sinha, V., Xu, X.: Tropospheric Ozone Assessment  
 877 Report: Present-day tropospheric ozone distribution and trends relevant to vegetation. *Elementa: Science of the*  
 878 *Anthropocene*; 6 47, <https://doi.org/10.1525/elementa.302>, 2018.
- 879
- 880 Monks, P. S., Archibald, A. T., Colette, A., Cooper, O., Coyle, M., Derwent, R., ... and Williams, M. L.: Tropospheric ozone  
 881 and its precursors from the urban to the global scale from air quality to short-lived climate forcer. *Atmospheric chemistry*  
 882 *and physics*, 15(15), 8889–8973. <https://doi.org/10.5194/acp-15-8889-2015>, 2015.
- 883
- 884 Pastorello, G., Trotta, C., Canfora, E.: The FLUXNET2015 dataset and the ONEFlux processing pipeline for eddy  
 885 covariance data. *Sci Data* 7, 225, <https://doi.org/10.1038/s41597-020-0534-3>, 2020.
- 886
- 887 Pieber, S.M., Henne, S., Nguyen, N.A., Nguyen, D.L., Steinbacher, M.: Trace Gases and Air Quality in Northwestern  
 888 Vietnam During Recurrent Biomass Burning on the Indochina Peninsula Since 2014—Field Observations and Atmospheric  
 889 Simulations. In: Vadrevu, K.P., Ohara, T., Justice, C. (eds) *Vegetation Fires and Pollution in Asia*. Springer, Cham.  
 890 [https://doi.org/10.1007/978-3-031-29916-2\\_32](https://doi.org/10.1007/978-3-031-29916-2_32), 2023.
- 891
- 892 Pleim, J. and Ran, L.: Surface flux modeling for air quality applications. *Atmosphere*, 2(3), pp.271–302.  
 893 <https://doi.org/10.3390/atmos2030271>, 2011.
- 894
- 895 Poyatos, R., Granda, V., Flo, V., Adams, M. A., Adorján, B., Aguadé, D., ... and Van Der Tol, C.: Global transpiration data  
 896 from sap flow measurements: the SAPFLUXNET database. *Earth System Science Data*, 13, 2607–2649,  
 897 <https://doi.org/10.5194/essd-13-2607-2021>, 2021.
- 898
- 899 Putaud J.P., Bergamaschi, P., Bressi, M., Cavalli, F., Cescatti, A., Daou, D., Dell’Acqua, A., Douglas, K., Duerr, M.,  
 900 Fumagalli, I., Goded, I., Grassi, F., Gruening, C., Hjorth, J., Jensen, N. R., Lagler, F., Manca, G., Martins Dos Santos, S.,  
 901 Matteucci, M., Passarella, R., Pedroni, V., Pokorska, O., Roux, D.: JRC – Ispra Atmosphere - Biosphere - Climate  
 902 Integrated monitoring Station: 2014 Report; EUR 27639 EN, <https://doi.org/10.2788/570407>, 2014.





903

904 Ran, L., Pleim, J., Song, C., Band, L., Walker, J.T. and Binkowski, F.S.: A photosynthesis-based two-leaf canopy stomatal  
 905 conductance model for meteorology and air quality modeling with WRF/CMAQ PX LSM. *Journal of Geophysical Research:*  
 906 *Atmospheres*, 122(3), pp.1930-1952, <https://doi.org/10.1002/2016JD025583>, 2017.

907

908 Raghav, P., Kumar, M., and Liu, Y.: Structural constraints in current stomatal conductance models preclude accurate  
 909 estimation of evapotranspiration and its partitions, <https://doi.org/10.1029/2024WR037652>, 2023.

910

911 Ramya, A., Dhevagi, P., Poornima, R., Avudainayagam, S., Watanabe, M., and Agathokleous, E.: Effect of ozone stress on  
 912 crop productivity: A threat to food security. *Environmental Research*, 116816. <https://doi.org/10.1016/j.envres.2023.116816>,  
 913 2023.

914

915 Savi, F. and Fares, S.: Ozone dynamics in a Mediterranean Holm oak forest: comparison among transition periods  
 916 characterized by different amounts of precipitation. *Annals of Silvicultural Research* 38(1) 1-6  
 917 <http://dx.doi.org/10.12899/ASR-801>, 2014

918

919 Schröder, S., Schultz, M. G., Selke, N., Sun, J., Ahring, J., Mozaffari, A., Romberg, M., Epp, E., Lensing, M., Apweiler, S.,  
 920 Leufen, L. H., Betancourt, C., Hagemeyer, B., Rajveer, S.: TOAR Data Infrastructure,  
 921 <https://doi.org/10.34730/4d9a287dec0b42f1aa6d244de8f19eb3>, 2021.

922

923 Schucht, S., Tognet, F., Létinois, L. and Ineris, I.N.: Wheat yield loss in 2019 in Europe due to ozone exposure, Eionet  
 924 Report-ETC/ATNI, 2021.

925

926 Silva, S. J. and Heald, C. L.: Investigating dry deposition of ozone to vegetation. *Journal of Geophysical Research:*  
 927 *Atmospheres*, 123(1), 559-573. <https://doi.org/10.1002/2017JD027278>, 2018.

928

929 Stella, Patrick, et al.: Predicting and partitioning ozone fluxes to maize crops from sowing to harvest: the Surf-atm-O 3  
 930 model, *Biogeosciences* 8.10, 2869-2886. <https://doi.org/10.5194/bg-8-2869-2011>, 2011.

931

932 Stella, P., Personne, E., Lamaud, E., Loubet, B., Trebs, I., & Cellier, P. (2013). Assessment of the total, stomatal, cuticular,  
 933 and soil 2 year ozone budgets of an agricultural field with winter wheat and maize crops, *Journal of Geophysical Research:*  
 934 *Biogeosciences*, 118(3), 1120-1132, <https://doi.org/10.1002/jgrg.20094>, 2013.

935



- 936 Sofen, E. D., Bowdalo, D., Evans, M. J., Apadula, F., Bonasoni, P., Cupeiro, M., ... and Tørseth, K.: Gridded global surface  
 937 ozone metrics for atmospheric chemistry model evaluation. *Earth System Science Data*, 8(1), 41-59,  
 938 <https://doi.org/10.5194/essd-8-41-2016>, 2016.
- 939
- 940 Sun, S., Tai, A. P. K., Yung, D. H. Y., Wong, A. Y. H., Ducker, J. A., and Holmes, C. D.: Influence of plant ecophysiology  
 941 on ozone dry deposition: comparing between multiplicative and photosynthesis-based dry deposition schemes and their  
 942 responses to rising CO<sub>2</sub> level, *Biogeosciences*, 19, 1753–1776, <https://doi.org/10.5194/bg-19-1753-2022>, 2022.
- 943
- 944 Tai, A. P., Yung, D. H., & Lam, T. : Terrestrial Ecosystem Model in R (TEMIR) version 1.0: simulating ecophysiological  
 945 responses of vegetation to atmospheric chemical and meteorological changes. *Geoscientific Model Development*, 17(9),  
 946 3733-3764, <https://doi.org/10.5194/gmd-17-3733-2024>, 2024.
- 947
- 948 Travis, K. R. and Jacob, D. J.: Systematic bias in evaluating chemical transport models with maximum daily 8 h average  
 949 (MDA8) surface ozone for air quality applications: a case study with GEOS-Chem v9. 02. *Geoscientific Model*  
 950 *Development*, 12(8), 3641-3648. <https://doi.org/10.5194/gmd-12-3641-2019>, 2019.
- 951
- 952 UNECE LRTAP (2017). III. Mapping critical levels for vegetation. Available at:  
 953 [https://icpvegetation.ceh.ac.uk/sites/default/files/FinalnewChapter3v4Oct2017\\_000.pdf](https://icpvegetation.ceh.ac.uk/sites/default/files/FinalnewChapter3v4Oct2017_000.pdf)
- 954 Visser, A. J., Ganzeveld, L. N., Goded, I., Krol, M. C., Mammarella, I., Manca, G., and Boersma, K. F.: Ozone deposition  
 955 impact assessments for forest canopies require accurate ozone flux partitioning on diurnal timescales, *Atmos. Chem. Phys.*,  
 956 21, 18393–18411, <https://doi.org/10.5194/acp-21-18393-2021>, 2021.
- 957
- 958 Walker, A. P., Quaife, T., Van Bodegom, P. M., De Kauwe, M. G., Keenan, T. F., Joiner, J., ... & Woodward, F. I.: The  
 959 impact of alternative trait-scaling hypotheses for the maximum photosynthetic carboxylation rate ( $V_{Cmax}$ ) on global gross  
 960 primary production. *New Phytologist*, 215(4), 1370-1386, <https://doi.org/10.1111/nph.14623>, 2017:
- 961
- 962 Wang, T., Wang, F., Song, H., Zhou, S., Ru, X. and Zhang, H.: Maize yield reduction and economic losses caused by  
 963 ground-level ozone pollution with exposure-and flux-response relationships in the North China Plain. *Journal of*  
 964 *Environmental Management*, 324, p.116379. <https://doi.org/10.1016/j.jenvman.2022.116379>, 2022.
- 965
- 966 Wilkinson, M. D., Dumontier, M., Aalbersberg, I. J., Appleton, G., Axton, M., Baak, A., ... & Mons, B.: The FAIR Guiding  
 967 Principles for scientific data management and stewardship. *Scientific data*, 3(1), 1-9.



968 <https://doi.org/10.1038/sdata.2016.18>, 2016.

969

970 Wong, A. Y. H., Geddes, J. A., Ducker, J. A., Holmes, C. D., Fares, S., Goldstein, A. H., et al.: New evidence for the  
 971 importance of non-stomatal pathways in ozone deposition during extreme heat and dry anomalies. *Geophysical*  
 972 *ResearchLetters*, 49, e2021GL095717, <https://doi.org/10.1029/2021GL095717>, 2022.

973

974 Yen M-Ch. , Peng C-M., Chen T.-C., Chen Ch.-S., Lin N.-H., Tzeng R.-Y., Lee Y.-A. , Lin Ch.-Ch.: Climate and weather  
 975 characteristics in association with the active fires in northern Southeast Asia and spring air pollution in Taiwan during 2010  
 976 7-SEAS/Dongsha Experiment, *Atmospheric Environment*, Volume 78, Pages 35-50,  
 977 <https://doi.org/10.1016/j.atmosenv.2012.11.015>, 2013.

978

979 Young, P. J.; Naik, V.; Fiore, A. M.; Gaudel, A.; Guo, J.; Lin, M.; Neu, J.; Parrish, D.; Rieder, H.;Schnell, J. others.:  
 980 Tropospheric Ozone Assessment Report: Assessment of Global-Scale Model Performance for Global and Regional Ozone  
 981 Distributions, Variability, and Trends. *Elem Sci Anth*, 6 (1), <https://doi.org/10.1525/elementa.265>, 2018.

982

983 Zhang, L., Brook, J. R., and Vet, R.: A revised parameterization for gaseous dry deposition in air-quality models, *Atmos.*  
 984 *Chem. Phys.*, 3, 2067–2082, <https://doi.org/10.5194/acp-3-2067-2003>, 2003.

985

986 Zhang, W., Feng, Z., Wang, X., Liu, X., & Hu, E.: Quantification of ozone exposure-and stomatal uptake-yield response  
 987 relationships for soybean in Northeast China. *Science of the Total Environment*, 599, 710-720,  
 988 <https://doi.org/10.1016/j.scitotenv.2017.04.231>, 2017.

989

990

991

992

993

994

995

996

997

998



999

## 1000 Appendix

### 1001 Table A1: Abbreviations

Symbol	Long name
rsmin	Minimum stomatal resistance in [ $\text{s m}^{-1}$ ]
gsmax	Maximum stomatal conductance in [ $\text{m s}^{-1}$ ]
RH	Relative humidity in [%]
LAI	Leaf area index in [ $\text{m}^2 \text{m}^{-2}$ ]
sd, sn	snow depth in [m] and snow cover
ssrd, strd	solar and thermal flux at surface in [ $\text{W m}^{-2}$ ]
sw	Soil wetness [m]
al_vis:	albedo (visible)
cwv	canopy water content in [ $\text{kg m}^{-2}$ ]
SWC	Soil water content
SM	Soil moisture [ $\text{m}^3 \text{m}^{-3}$ ]
wdir	geo wind direction [ $^\circ$ ]
wspeed	Wind speed in [ $\text{ms}^{-1}$ ]
cv	Vegetation fraction [ $\text{m}^2 \text{m}^{-2}$ ]
P	Precipitation in [mm]
P_rate	Precipitation rate in [ $\text{mm h}^{-1}$ ], [ $\text{kg m}^{-2} \text{s}^{-1}$ ], [ $\text{m s}^{-1}$ ]



Tair, Tsoil, T2m	Air, soil, 2m temperature in [K]
VPD	Vapour pressure deficit [kPa]
Pa	Air pressure [hPa]
Rn, Gr	Net and global radiation [ $\text{W m}^{-2}$ ]
$u^*$	Friction velocity [ $\text{m s}^{-1}$ ]
O <sub>3</sub> , CO <sub>2</sub>	O <sub>3</sub> and CO <sub>2</sub> concentration in [ppb] und [ppt]
h <sub>dis</sub> , z <sub>0</sub>	Displacement height [m], roughness length [m]
CF	Cloud fraction
LUC	Land usage category

1002

1003